# A Comparison of B-spline Surface and Free-form Deformation Geometry Control Methods for Aerodynamic Shape Optimization

by

Christopher Soo Tiong Lee

A thesis submitted in conformity with the requirements
for the degree of Master of Applied Science
Graduate Department of Aerospace Science and Engineering
University of Toronto

# Abstract

A Comparison of B-spline Surface and Free-form Deformation Geometry Control Methods for Aerodynamic Shape Optimization

Christopher Soo Tiong Lee
Master of Applied Science
Graduate Department of Aerospace Science and Engineering
University of Toronto
2015

The priority of designing fuel-efficient aircraft is motivated by both environmental and financial factors. One key approach is to minimize drag using aerodynamic shape optimization. By coupling a computational fluid dynamics solver with an optimization algorithm, a thorough yet efficient search of the design space can be conducted to find an optimal design, which may be a novel shape. The ability to find such a design, however, is determined by the geometry parameterization and control method employed. As such, two geometry control methods currently in use in the Computational Aerodynamics group at UTIAS, B-spline surface control and free-form deformation, are compared. The control methods are evaluated on the basis of the quality of the optimized shape as well as the ease of use for problem setup. The methods are applied to a suite of benchmark problems defined by the AIAA Aerodynamic Design Optimization Discussion Group, as well as to two additional cases, which range from two dimensional to three dimensional, subsonic to transonic, and inviscid to viscous and turbulent. B-spline surface optimization is often found to result in slightly lower drag; however in general both methods perform equally well, especially when optimized geometries are evaluated on finer grids. The exception is in the case of a dihedral and sectional optimization, where convergence paths taken by the two geometry control methods are significantly different and the B-spline surface optimization reduces drag more effectively. Free-form deformation provides a more general approach to problem setup.

# Acknowledgements

I would like to begin by thanking Professor David Zingg for being an exceptional supervisor. His insight and input were not only invaluable in moving me forward with my research, but also challenged me to think more deeply about each problem I encountered, and motivated me to seek to produce the highest quality of work. I would also like to thank my research assessment committee members, Professor Prasanth Nair and Professor Craig Steeves, for their insightful comments and suggestions as I progressed through the project.

I am grateful for the UTIAS community and in particular, the CFD lab, for providing a professional, yet welcoming and enjoyable environment to be a part of these past two years. I would like to thank Howard for the tutorials on the group's code that helped me hit the ground runnning, Hugo for teaching me the ins and outs of FFD and for his continual input along the way, Shahriar for investing so much time into providing me with thorough explanations for concepts I was struggling with, and Tom for helping me think through problems systematically when I felt stuck.

I am so thankful for my family, who have blessed me with more love, encouragement, and support throughout my life than I could ever ask for. I would not be who or where I am today without them.

Tanya, thank you for motivating me when I felt like my efforts were not amounting to anything, for helping me laugh when I was discouraged, for patiently loving me even when school was consuming my mind, for being with me every step of the way. I am so blessed to have you by my side.

Finally, I thank my God and Saviour Jesus Christ. Every skill, opportunity, and success I have ever had has been a gift from you. May I only ever use what you have blessed me with to honour, pursue, and love you.

CHRISTOPHER SOO TIONG LEE

University of Toronto Institute for Aerospace Studies
May 6, 2015

# Contents

# List of Tables

# List of Figures

# List of Symbols and Abbreviations

### Alphanumeric

| | |
|---|---|
| $\mathbf{\Lambda}$ | Lagrange multipliers (adjoint variables) |
| $\mathcal{J}$ | Objective function |
| $\mathcal{L}$ | Lagrangian function |
| $\mathcal{M}$ | Mesh residuals |
| $\mathcal{N}$ | B-spline basis function |
| $\mathcal{R}$ | Flow residuals |
| $\mathbf{A}$ | Displaced surface control-point coordinates |
| $\mathbf{B}$ | General B-spline coordinates |
| $\mathbf{b}$ | Volume control-point coordinate vector |
| $\mathbf{b}_{\text{srf}}^{(i)}$ | Surface control-point coordinate vector at mesh movement increment $i$ |
| $\mathbf{q}$ | Flow variables |
| $\mathbf{t}$ | Physical world space |
| $\mathbf{v}$ | Design variable vector |
| $A$ | Area |
| $c$ | Chord length |
| $C_d$, $C_D$ | 2D, 3D drag coefficient |
| $C_l$, $C_L$ | 2D, 3D lift coefficient |
| $C_m$, $C_M$ | 2D, 3D pitching moment coefficient |
| $C_p$ | Pressure coefficient |
| $M$ | Mach number |

| | |
|---|---|
| $m$ | Total mesh movement increments |
| $p$ | B-spline degree |
| $Re$ | Reynolds number |
| $S$ | Reference area |
| $T$ | B-spline knot vector |
| $t$ | Sectional thickness |
| $V$ | Volume |
| $x$, $y$, $z$ | Cartesian coordinate directions |
| $y^+$ | Nondimensional off-wall distance |

**Greek**

| | |
|---|---|
| $\alpha$ | Angle of attack |
| $\boldsymbol{\xi} = \xi, \eta, \zeta$ | Parametric coordinates |
| $\Gamma$ | Dihedral |
| $\gamma$ | Twist |

**Abbreviations**

| | |
|---|---|
| ADODG | Aerodynamic Design Optimization Discussion Group |
| ASO | Aerodynamic shape optimization |
| BWB | Blended wing-body |
| CFD | Computational fluid dynamics |
| CRM | Common research model |
| DV | Design variable |
| FFD | Free-form deformation |
| ICAO | International Civil Aviation Organization |
| MAC | Mean aerodynamic chord |
| RANS | Reynolds-averaged Navier-Stokes |
| SNOPT | Sparse Nonlinear OPTimizer |

# Chapter 1

# Introduction

## 1.1 CFD and Aerodynamic Shape Optimization

THE dual forces of growing concern over the negative impact of carbon emissions in the environment and the rise of jet fuel prices pressure aircraft manufacturers to prioritize minimizing fuel burn when designing new aircraft. In 2012, commercial flights transported close to 3 billion passengers around the world [4]. In the process, 72 billion gallons of jet fuel were consumed, releasing 682 million tonnes of $CO_2$ emissions into the atmosphere [5], accounting for 2% of humanity's annual carbon emissions. While this percentage may seem small, it is expected that the annual number of passengers will double by 2030 [4], increasing the potential impact on the environment. In an effort to minimize the aircraft industry's environmental footprint, the industry has committed to "improving fuel efficiency an average of 1.5% annually to 2020, capping net emissions through carbon-neutral growth from 2020, [and] cutting net emissions in half by 2050, compared with 2005." [6] At the same time, fuel costs have more than doubled between 2004 and 2013, and can now account for 31% of an airline's operating costs [6]. Even with the recent drop in fuel prices, they remain volatile, and the operation of fuel-efficient aircraft is key to ensuring the profitability of airlines. In short, continual improvements in fuel efficiency are required to ensure both environmental and economic sustainability of air transport.

The industry's strategy for dealing with these challenges includes advancing technology to improve the efficiency of aircraft, improving operations to fly smarter, developing biofuels, and employing economic measures [6]. One key focus of technology advancement is improving aerodynamic performance through drag minimization using computational

fluid dynamics (CFD). On its own, a CFD solver is a tool capable of analyzing a single, specific design, but in recent years the rapid development of computing power has enabled the feasible use of computational design tools which have not only sped up, but drastically altered the design process. By coupling a CFD solver with an optimization algorithm and a geometry parameterization and control tool, designers are able to perform aerodynamic shape optimization (ASO), in which a given aerodynamic shape, such as a wing, is iteratively re-designed and re-analyzed, moving towards an optimal shape.

A typical ASO problem is defined by specifying the flow conditions, an objective function, design variables, and constraints. Flow condition specification may include indicating whether the flow is to be modelled as inviscid or viscous, laminar or turbulent, the Reynolds number in the viscous case, the Mach number, and the angle of attack. Example objective functions include drag minimization, lift-to-drag ratio maximization, and inverse design to recover a desired pressure distribution. Typical design variables include airfoil section changes, chord, twist, sweep, span, dihedral, and angle of attack. Constraints may include a lift target, minimum volume and projected area, or constraints to maintain a certain level of geometric smoothness. Solving an ASO problem provides an exploration of the design space at a fraction of the financial and time cost that would be needed for an experimental cut and try approach, or to manually alter models for separate numerical analyses. These tools allow not only for more robust fine tuning of existing designs, but also the exploration of unconventional configurations which may provide more dramatic aerodynamic improvements and for which much less design intuition and experience exist in the industry.

The importance of highly efficient and accurate CFD and optimization algorithms for the success of ASO is obvious. The CFD solver must be accurate enough to provide a good measure of the drag for a specific shape, while remaining efficient enough to allow for the analyses of a high number of designs in an acceptable time frame. Similarly, the optimization algorithm must provide the accuracy to achieve an optimum in a reasonable time frame, even in the presence of a design space defined by a high number of design variables. Another key component of ASO is the geometry control technique used to describe and control the shape of the geometry throughout the optimization. The geometry control method defines what shapes can actually be explored during the optimization. It must be flexible enough to handle both detailed local changes, such as airfoil section shape, and global shape changes, such as planform shape, to ensure the true optimum is achieved. As a result, much work has gone into developing different geometry parame-

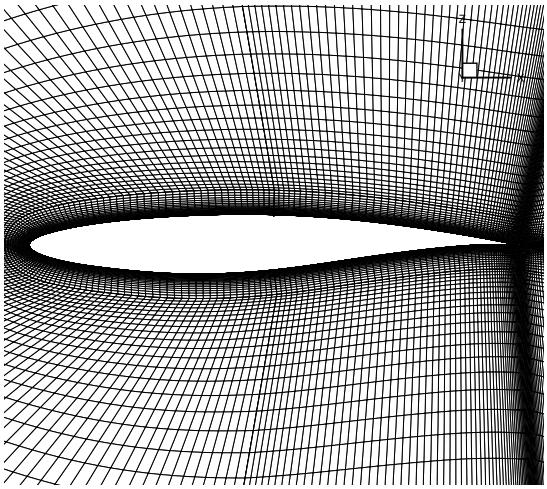

Figure 1.1: RAE 2822 grid showing a large number of surface node design variables

terization and control techniques [7, 8, 9]. Some of these geometry control methods are outlined next.

## 1.2 Brief Review of Geometry Control Methods

A distinction is first made between geometry parameterization and geometry control. A geometry parameterization describes how the geometry is defined in physical space. The definition may come in the form of an analytical function, which generally provides a continuous geometry, or in the form of discrete points, as in the surface grid nodes, for example. The geometry control method defines how changes are applied to the geometry parameterization, i.e. how the design variables for optimization are defined. Design variables may be defined explicitly in terms of the geometry parameterization, in which case the parameterization and control are directly coupled. On the other hand, design variables may also be defined such that they describe deformations to the geometry without explicitly defining the underlying geometry itself.

Perhaps the most obvious geometry control approach is the discrete approach, in which coordinates on the surface itself (for example, grid nodes or airfoil section data) directly define the surface and are the design variables [10]. This provides good local control and the simplicity of being able to use the computational grid without any additional parameterization, but can suffer from high cost for a dense surface grid, as well as poor smoothness. A typical 2D mesh for an RAE 2822 airfoil is displayed in Figure 1.1. One can imagine that allowing all of the surface grid nodes to move independently

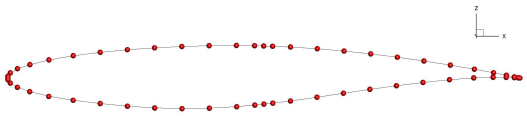

Figure 1.2: RAE 2822 controlled by red B-spline surface control points

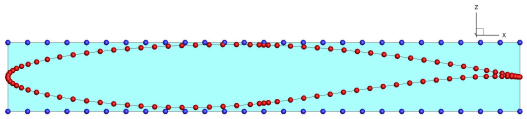

Figure 1.3: RAE 2822 embedded in light blue FFD volume and controlled by dark blue FFD control points

is excessive.

The number of design variables can be reduced through the use of polynomial or spline approaches. In particular, B-spline curves are popular, since they can parametrize complex geometries efficiently and accurately [11]. In addition, the more general non-uniform rational B-splines (NURBS) are able to exactly define implicit conic sections [12]. The same airfoil from Figure 1.1 is shown in Figure 1.2, now controlled by the red B-spline control points, which are clearly fewer in number than the grid nodes.

Free-form deformation (FFD), first formally introduced by Sederberg and Parry [2], is an approach taken from the soft object animation industry. It can be visualized by embedding a flexible object of interest inside a flexible volume, and deforming both of them simultaneously by deforming the lattice of the volume. Since this is a volume-based parameterization, its applications can be extended to consider structural deformations in multidisciplinary design optimization. The RAE 2822 airfoil is shown in Figure 1.3, now enclosed in a light blue volume controlled by the dark blue FFD control points.

Another geometry control approach is the PARSEC method [1] which employs 11 parameters to define an airfoil. These parameters, such as leading-edge radius and trailing-edge angles, are of physical interest to designers, making this method popular for its intuitive concept, but it is overly restrictive for the purposes of exploratory design. The design variables provided by the PARSEC method are displayed in a diagram from Sobieczky [1] in Figure 1.4.

The MASSOUD approach [13] also takes the approach of defining design variables such as thickness and camber, but parametrizes perturbations to the shape instead of

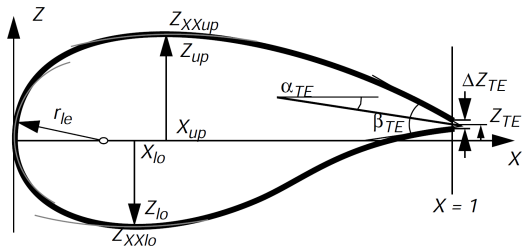


Figure 1.4: PARSEC airfoil design variables (Used with permission) [1]

the actual geometry. The deformed grid $\bar{R}(\bar{v})$ is given by

$$\bar{R}(\bar{v}) = \bar{r} + \Delta\bar{R}(\bar{v}) \tag{1.1}$$

where $\bar{r}$ is the initial grid, $\Delta\bar{R}$ is the perturbation, and $\bar{v}$ is vector of design variables. The perturbation $\Delta\bar{R}$ is given by

$$\Delta\bar{R} = \delta\bar{R}_{\text{th}} + \delta\bar{R}_{\text{ca}} + \delta\bar{R}_{\text{tw}} + \delta\bar{R}_{\text{sh}} + \delta\bar{R}_{\text{pl}} \tag{1.2}$$

where each term is a function defining thickness, camber, twist, shear, and planform, respectively.

Analytical approaches add shape functions to a reference geometry. For example, Hicks-Henne "bump" functions [14] add weighted sine function perturbations to a baseline geometry $z_{\text{init}}$ to produce a new geometry $z$:

$$z = z_{\text{init}} + \sum_{i=1}^{N} \alpha_i f_i(x) \tag{1.3}$$

where $\alpha_i$ are the design variables and are weights controlling the contributions of the bump functions, which are given by

$$f_i(x) = \left[\sin\left(\pi x^{\frac{\log 0.5}{\log t_1}}\right)\right]^{t_2}, 0 \leq x \leq 1, \tag{1.4}$$

where $t_1$ dictates the location of the peak, and $t_2$ dictates the width of the bump.

This is by no means a comprehensive list of all geometry control options available, and the reader is encouraged to consult Samarah [7] for more details.

B-spline surface control is one of the more popular methods currently in use, and has been applied extensively and successfully in the author's research group in 2D [15] and 3D [16]. In addition, Gagnon and Zingg [17] have recently developed a novel FFD approach of embedding the surface control points in the FFD volume, which maintains

the analytical definition of the geometry exactly, as opposed to the usual approach of embedding the grid nodes [18, 19, 20, 21]. The method's robustness was demonstrated in deforming a sphere into a blended wing-body [22]. The implementation also features the inclusion of an axial curve to which the FFD volume is attached. The axial curve, whose mathematical definition is decoupled from that of the FFD volume, provides an intuitive way to make large scale changes to the FFD volume.

Naturally, the question arises as to which geometry control method is preferred for high-fidelity aerodynamic shape optimization, in particular exploratory optimization where substantial shape changes are permitted. Amoiralis and Nikolos [23] conducted a comparison between FFD and B-spline surface control and found that FFD generally led to a greater reduction of the cost function for a comparable number of design variables for a series of inverse optimizations. The optimizations conducted, however, were only 2D inverse problems and used a low-fidelity solver [24]. Therefore, a more thorough comparison using high-fidelity CFD is necessary.

## 1.3 Thesis Objectives

Given the two methods of geometry control, B-spline surface control and FFD, the purpose of this project is to perform a detailed comparison of the two techniques to determine the limitations and advantages of each. It is not expected that one approach will be found to be superior in all situations, but rather that each will have its advantages in different cases. Hence, the objective of this study is to provide a thorough understanding of which method is preferred for certain classes of problems, i.e. for certain geometries, flow conditions, or design objectives.

The comparison study between the two geometry control methods will be conducted by evaluating the methods on the bases of:

- Quality of final shape (objective function value)
- Robustness in dealing with different classes of problems (2D, 3D; Euler, Reynolds-averaged Navier-Stokes (RANS); subsonic, transonic; small refinements, large shape changes)
- Ease of use (e.g. implementation of constraints)

To provide a basis for comparison, four benchmark cases from the AIAA Aerodynamic Design Optimization Discussion Group (ADODG) are considered. These cases were chosen by researchers in the aerodynamic design optimization community to allow research groups from industry and academia to test and compare their codes under a variety of aerodynamic shape optimization problems. A range of flow conditions and geometric flexibility are considered. As such, these were deemed to be suitable cases for geometry control method comparison. The optimization problems include the following:

- Case 1: Euler drag minimization of a modified NACA 0012 airfoil at Mach number $M = 0.85$ and zero angle of attack $\alpha$, with thickness constrained to be greater than or equal to the baseline thickness

- Case 2: RANS lift-constrained drag minimization of the RAE 2822 airfoil at $M = 0.734$, lift coefficient $c_l = 0.824$, moment coefficient $c_m \geq -0.092$, and Reynolds number $Re = 6.5 \times 10^6$

- Case 3: Euler lift-constrained drag minimization of a rectangular wing with a NACA 0012 section, allowing only twist distribution changes, at $C_L = 0.375$ and $M = 0.5$

- Case 4: RANS lift-constrained drag minimization of a wing from the Common Research Model (CRM) wing-body configuration of the Fifth Drag Prediction Workshop, allowing section, twist, and angle of attack changes, at $C_L = 0.5$, $C_M \geq -0.17$, $M = 0.85$, and $Re = 5 \times 10^6$

In addition to these benchmark cases, two additional optimization cases are considered, which allow increased geometric flexibility. These include the following:

- Case 5: RANS lift-to-drag ratio maximization of a blended wing-body (BWB) configuration, allowing section, twist, planform, and angle of attack changes, at $M = 0.80$ and $Re = 62 \times 10^6$

- Case 6: RANS lift-constrained drag minimization of a nonplanar swept wing, allowing nonlinear dihedral, sectional, and angle of attack changes, at $C_L = 0.5$, $M = 0.78$, and $Re = 23.5 \times 10^6$

## 1.4 Summary of Past Results for Benchmark Cases

The ADODG has convened twice so far, and at each meeting, participants have presented results for the first four cases that will be explored in this thesis. While a full review containing each participant's results for each test case is beyond the scope of this report, some key findings for each case are summarized below to place the present work in context.

Case 1 is based on the work of Vassberg et al. [25] A Bezier curve parameterization was used, and the impact of dimensionality was investigated by increasing the number of design variables per surface from 0 to 36. Increasing the dimensionality of the design space enabled further drag reduction, and the best result was achieved using 36 design design variables per surface, reducing the drag from 468.9 to 103.8 counts. It was noted at the end of this paper that final designs appeared unstable when the Mach number was perturbed, leading to an investigation by Jameson et al. [26]. The final geometry from Vassberg et al. [25], along with three other blunt airfoils, were demonstrated to give non-unique solutions by initializing the zero angle of attack flow solution with a flow field from a slightly perturbed angle of attack. The resulting warm-started solutions gave non-zero lift and higher drag than the zero lift solutions. Hysteresis plots over angle of attack were produced. Further investigations of non-uniqueness with these blunt airfoils were conducted to investigate unsteady, viscous flow [27] and finite-wings [28].

Despite the apparent ill-posedness of the problem, this optimization case has been included in the ADODG test suite and has been conducted by numerous research groups. Telidetzki et al. [29] used 8 design variables per surface to reduce the drag from 425 to 61 counts. Lee et al. [30] improved upon this result by optimizing on a finer mesh, reducing drag from 457 to 42 counts using 9 design variables per surface. Non-unique solutions consistent with Jameson et al. [26] were observed to not only affect analysis of the final design, but inhibit optimization convergence. Bisson et al. [31] used B-spline control points for geometry control. Using 14 design variables per surface, they reduced the drag from 464 to 44 drag counts when analyzed on a superfine mesh. Grid refinement studies for the initial and final geometries showed the numerical error increasing significantly for the final geometry. Bisson and Nadarajah [32] improved upon this result by enforcing a symmetric boundary condition in the wake-cut, which helped alleviate some of the convergence difficulties from the non-unique solutions and allowed drag reduction to 25 counts. Anderson et al. [33] employed an adaptive mesh refinement approach and

progressive parameterization refinement to reduce numerical error and increase geometric flexibility in an efficient manner, reducing drag from 471 to 43 counts. LeDoux et al. [34] employed multiple flow solvers and optimization frameworks to demonstrate the sensitivity of the results for this case to the tools and grids used. Lifting solutions were also observed. Méheut et al. [35] performed a cross validation study using optimized geometries from several participants in the ADODG and produced Mach hysteresis plots demonstrating the non-unique nature of the solutions for all of the optimized geometries.

Bisson et al. [31] performed Case 2 using B-spline surface control and reduced the drag from 166 to 102 counts using 6 design variables per surface. As with Case 1, LeDoux et al. [34] used multiple CFD and optimization tools to demonstrate significant sensitivity of the results to the methodology employed. Hysteresis behaviour over different angles of attack was observed, again giving evidence of non-uniqueness in the design space.

Case 3 is based on the work of Hicken and Zingg [36]. With 15 spanwise B-spline control point stations, a span efficiency factor of 0.994 and a lift distribution very close to elliptical were achieved. Gagnon and Zingg [17] achieved a span efficiency factor of 0.9995 using 10 FFD twist stations. In this case, the initial geometry had a slightly reduced span and airfoil sections were twisted by rotation rather than shearing to maintain constant projected chord.

Case 4 is based on the work of Osusky et al. [37], who used 8 chordwise by 11 spanwise surface control points on the upper and lower surfaces of the CRM wing and reduced the drag from 197 to 186 counts. Telidetzski et al. [29] showed that increasing the number of spanwise stations from 11 to 16 provides minimal additional drag reduction. Lyu et al. [18] used an FFD of 24 chordwise by 15 spanwise by 2 vertical control points and a multilevel optimization acceleration approach to reduce the drag from 199 to 182 counts. A multimodality study that initialized a series of optimizations from perturbed geometries revealed multiple local minima within 0.1 drag counts of each other.

## 1.5 Thesis Outline

The remainder of the thesis is organized as follows: Chapter 2 summarizes the algorithms employed in the aerodynamic design optimization framework called Jetstream. Chapter 3 presents the results obtained for the four benchmark problems, as well as for the BWB and nonplanar optimizations. Chapter 4 outlines conclusions and recommended future work.

# Chapter 2

# Methodology

AERODYNAMIC shape optimization codes are typically composed of three main components: a geometry parameterization and control methodology, which typically includes mesh movement, a flow solver, and an optimization algorithm, with gradient computation if needed. Herein lies a brief description of each component in the context of Jetstream.

## 2.1 Integrated Geometry Parameterization, Control, and Mesh Movement

### 2.1.1 B-Spline Mathematics

A fundamental understanding of B-splines is needed, as they form the building blocks of both geometry control methods studied in this project. A B-spline curve of degree $p$ is defined as the linear combination of basis functions $\mathcal{N}_i^{(p)}$ weighted with control-point coordinates $\{\mathbf{B}_i\}_{i=1}^N$:

$$\mathbf{C}(\xi) = \sum_{i=0}^{N} \mathcal{N}_i^{(p)}(\xi)\mathbf{B}_i \quad a \leq \xi \leq b. \tag{2.1}$$

The basis functions are functions of computational coordinates $\xi$ and are joined at the knot locations defined by the knot vector

$$T = \{\underbrace{a, ..., a}_{p+1}, \xi_{p+1}, ..., \xi_N, \underbrace{b, ...b}_{p+1}\}. \tag{2.2}$$

The $p+1$ repeating knots at the ends of the vector ensure that the curve passes through $\mathbf{B}_1$ and $\mathbf{B}_N$. The B-spline basis functions are defined recursively in terms of parameter

space and the knot vector as

$$\mathcal{N}_i^{(0)}(\xi) = \begin{cases} 1 & \text{if } \xi_i \leq \xi < \xi_{i+1} \\ 0 & \text{otherwise} \end{cases} \tag{2.3a}$$

$$\mathcal{N}_i^{(p)}(\xi) = \frac{\xi - \xi_i}{\xi_{i+p} - \xi_i}\mathcal{N}_i^{(p-1)}(\xi) + \frac{\xi_{i+p+1} - \xi}{\xi_{i+p+1} - \xi_{i+1}}\mathcal{N}_{i+1}^{(p-1)}(\xi). \tag{2.3b}$$

Extending these concepts to multidimensions, a B-spline surface or volume can be defined similarly as a tensor product, with a volume defined as

$$\mathbf{V}(\boldsymbol{\xi}) = \sum_{i=0}^{N_i}\sum_{j=0}^{N_j}\sum_{k=0}^{N_k}\mathcal{N}_i^{(p_i)}(\xi)\mathcal{N}_j^{(p_j)}(\eta)\mathcal{N}_k^{(p_k)}(\zeta)\mathbf{B}_{i,j,k}, \tag{2.4}$$

where $\boldsymbol{\xi} = (\xi, \eta, \zeta)$ are 3D parametric coordinates.

### 2.1.2 B-Spline Surface Geometry Parameterization and Control

#### Grid Fitting Procedure

Whether B-spline surface or FFD control is to be used for the optimization, each block in the multi-block structured mesh is fitted with a cubic B-spline volume with a specified number of control points. Cubic B-spline volumes are typically used, since they accurately and efficiently capture an initial geometry and provide good geometric flexibility.

The fitting procedure for a given block is described as follows [16]. The parametric values of the grid nodes $G = \{\mathbf{x}_{q,r,s} | q = 1, ...L_q, r = 1, ..., L_r, s = 1, ..., L_s\}$ are located based on a chord-length parameterization. For example, parameter $\xi_{q,r,s}$ is calculated along the grid line of constant $r = r_0$ and $s = s_0$ as

$$\xi_{1,r_0,s_0} = 0 \tag{2.5a}$$

$$\xi_{q,r_0,s_0} = \frac{1}{\Psi}\sum_{t=1}^{q-1}||\mathbf{x}_{t+1,r_0,s_0} - \mathbf{x}_{t,r_0,s_0}||, \quad q = 2, ..., L_q, \tag{2.5b}$$

where the normalization factor of total arc length is given by

$$\Psi = \sum_{t=1}^{L_q-1}||\mathbf{x}_{t+1,r_0,s_0} - \mathbf{x}_{t,r_0,s_0}||. \tag{2.6}$$

Next, the knot vectors are determined. To allow for a more accurate mapping, the knots are generalized to be spatially varying in parametric space. Bilinear knots have

been chosen for simplicity:

$$T_i(\eta,\zeta) = T_{i,(0,0)}(1-\eta)(1-\zeta) + T_{i,(1,0)}\eta(1-\zeta) + T_{i,(0,1)}(1-\eta)\zeta + T_{i,(1,1)}\eta\zeta. \quad (2.7)$$

The edge knots, for example $T_{i,(0,0)}$ for edge $(\xi,0,0)|\xi \in [0,1]$, are given by equations of the form

$$T_{i,(0,0)} = (\xi_{q+1,1,1} - \xi_{q,1,1})[\bar{q}_i - (q-1)] + \xi_{q,1,1}, \quad q-1 \le \bar{q}_i \le q, \quad (2.8)$$

where

$$\bar{q}_i = \left(\frac{L_q - 1}{N_i + 1 - p}\right)(i-p), \quad (2.9)$$

and $q$ is taken such that $q-1 \le \bar{q}_i \le q$. The number of grid node parameters in each knot span is almost the same, giving a B-spline control mesh of control points with clustering that mimics the spacing distribution of the computational mesh, i.e. the control mesh is a coarse approximation to the computational mesh.

The control-point coordinates are determined by solving a least-squares problem to best fit the initial volume grid, first for the block edges, then the faces, and then the interior. This ensures $C^0$ continuity of grid lines across the block interfaces. Again, this grid fitting procedure is conducted whether B-spline surface or FFD geometry control is used. The results of the fitting are an analytical B-spline surface definition of the geometry and a B-spline control grid that is used for the mesh movement, which is described later. Hyperbolic node distributions are used during mesh generation, and the analytical B-spline volumes describing each block allow for parametric grid refinement that preserves the hyperbolic distribution and gives refined grids of the same "family". Figure 2.1(a) displays an input grid for a blended wing-body (BWB) that is fitted to produce the B-spline control grid in Figure 2.1(b). The offwall spacing displayed in Figure 2.1(a) is too coarse to produce accurate drag prediction for the intended RANS analysis. Since the B-spline control-point clustering mimics the clustering of the input fitting grid, typical RANS meshes are prone to control point cross-over, causing either fitting or mesh-movement failures. A solution to this is to use a fitting grid with coarser offwall spacing and whose only purpose is to produce the original B-spline control grid. To generate the computational grid for flow analysis, an additional input grid with finer offwall spacing is provided, from which new grid node parameters are read and fed through the B-spline mapping to produce the analysis grid. This procedure can also be used to customize control-point distributions in other desired ways independent from the analysis grid and is sometimes used in Euler-based optimizations as well.

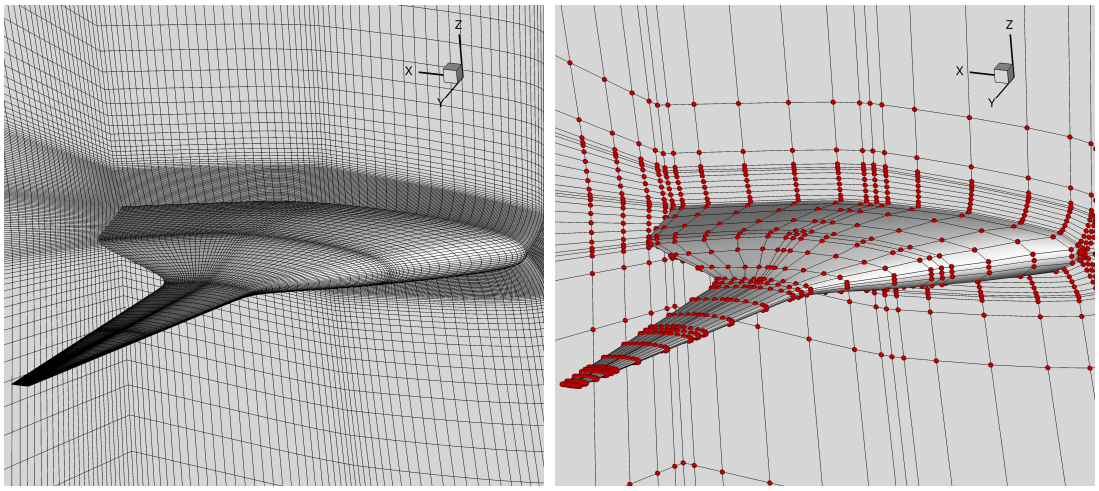


(a) Fitting mesh (b) B-spline control mesh

Figure 2.1: Surface and symmetry plane of a BWB fitting and B-spline control mesh, with B-spline control points in red

### B-spline Surface Control

If B-spline surface control is used, the control points defining the geometry's surface are taken as the design variables. Controlling the geometry using the surface control points can be thought of as manipulating the surface using puppet strings. The local support property of B-splines means that the influence of a single control point on the surface is localized. In general, each of these control points can have a degree-of-freedom in each of the three coordinate directions. To help optimization convergence by minimizing the number of design variables and prevent control point cross-over, and also to define design variables that are intuitive for aircraft design, certain degrees of freedom can be frozen or constrained into groups. For example, the $z$-directional freedom can be left free to define sectional design variables, but also constrained to define twist and dihedral design variables. The $x$-directional freedom is usually constrained to define chord and sweep design variables, the $y$-directional freedom to define span design variables. The block face defining a surface is sometimes called a surface patch. Control points around patch interfaces can be constrained to maintain desired levels of continuity, for example, $C^1$ or $C^2$ continuity. Figure 2.2 shows an initial and optimized BWB manipulated by red surface control points.

A generalized approach for dealing with B-spline surface design variables and con-

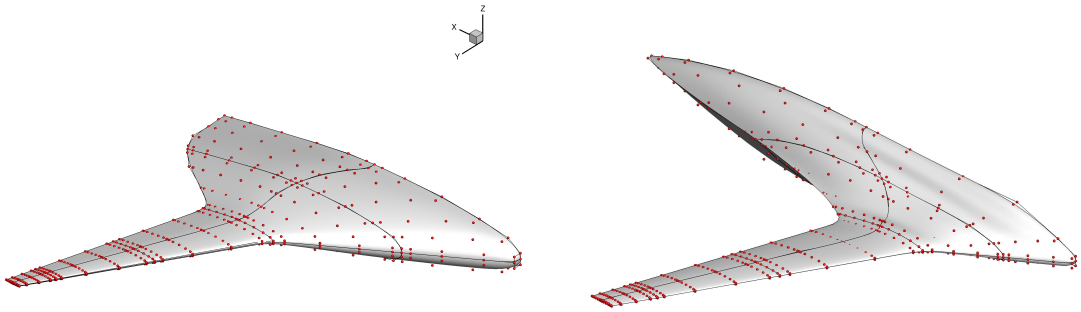

(a) Initial (b) Optimized

Figure 2.2: Planform of a BWB optimized using B-spline surface control

straints called region design variables has been developed [37] and is used for Cases 5 and 6 in this work. The region design variable approach was developed to enable the user to optimize a wide range of geometries without the need to implement customized design variable and constraint definitions. As long as the grid topology defines the wing in terms of upper and lower surfaces, as is the case for H-H- and H-O-topologies, surface patches can be grouped into sets called "regions". Design variables and constraints are defined for each region, allowing the user to simply turn flags on/off and set variable and constraint bounds. The B-spline surface is constrained to be $C^2$ continuous at surface patch interfaces that lie within a region, and can be constrained to be $C^1$ continuous at interfaces that lie between regions. Regions are further grouped into "components", for which higher level design variables and constraints may be defined. For example, a cranked wing may be defined by two regions: one inboard and one outboard of the crank. These two regions may form a single component. If the spans of the regions are free to change, but that of the component is fixed, then the location of the crank will be free to move while maintaining constant wing span.

### 2.1.3 Free-Form Deformation Geometry Control

Free-form deformation (FFD) is the second geometry control method to be considered. Figure 2.3, from Sederberg and Parry [2], illustrates the concept. The coloured spheres and cubes are embedded inside a translucent cube, which is the FFD volume. As the translucent cube is deformed, the embedded objects within are deformed with it.

In traditional aerodynamic design optimization practice, the embedded objects are the surface grid nodes [18, 19, 20, 21]. In Jetstream, however, the embedded objects are

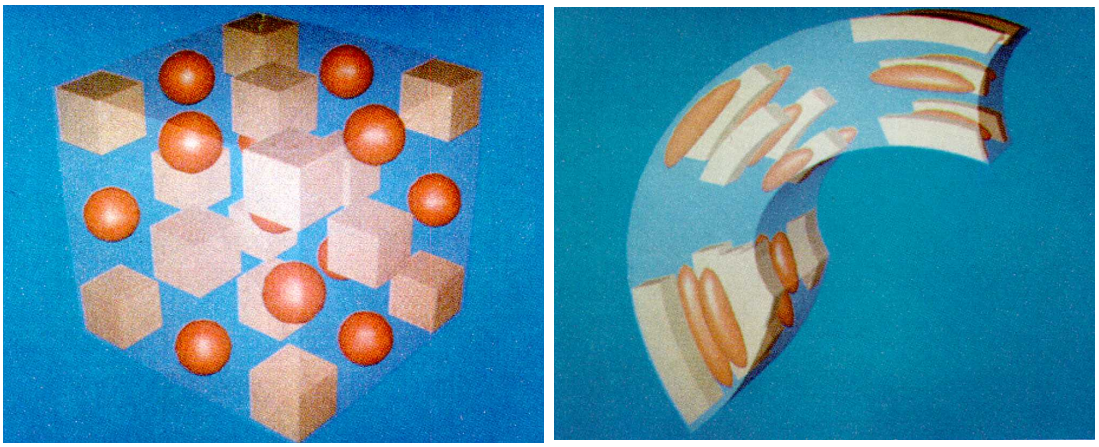

(a) Undeformed (b) Deformed

Figure 2.3: Conceptual illustration of FFD deformation (Used with permission) [2]

taken as the B-spline surface control points defining the geometry, and the FFD volume is a cubic B-spline volume [17]. This maintains an analytical definition of the geometry and allows the mesh movement, described later, to be performed in the same way as with B-spline surface control. The FFD volume is created using a geometry generation tool called GENAIR [38].

Numerically, FFD is executed using two functions. The first, $F^{-1}(\mathbf{t}) = \boldsymbol{\xi}$, is the embedding function and is evaluated only once. The coordinates of the surface control points are mapped from physical space $\mathbf{t}$ to the parametric space $\boldsymbol{\xi}$ of the FFD volume. This is accomplished using a Newton search algorithm. Referring back to Equation 2.4, the embedding function determines the $\xi, \eta, \zeta$ parametric coordinates of each embedded surface control point, and these coordinates remain unchanged during the optimization. The second function, $\tilde{F}(\boldsymbol{\xi}) = \tilde{\boldsymbol{t}}$, is the deformation function which algebraically evaluates the new coordinates in physical space of every embedded surface control point once the FFD volume has been deformed. Every time the optimizer adjusts the FFD control-point coordinates $\mathbf{B}_{i,j,k}$, the deformation function given by Equation 2.4 re-evaluates the surface control-point coordinates $\mathbf{V} = (x, y, z)$.

While B-spline surface control couples the design variables with the geometry parameterization, FFD decouples the two, parameterizing deformations rather than the geometry itself. So while the geometric design variables in the surface-based control approach are the surface control points, the geometric design variables in the FFD approach are a set of the FFD volume control points $\mathbf{v}_{\text{geo}} \in \{\mathbf{B}_{i,j,k}\}$. Gagnon and Zingg

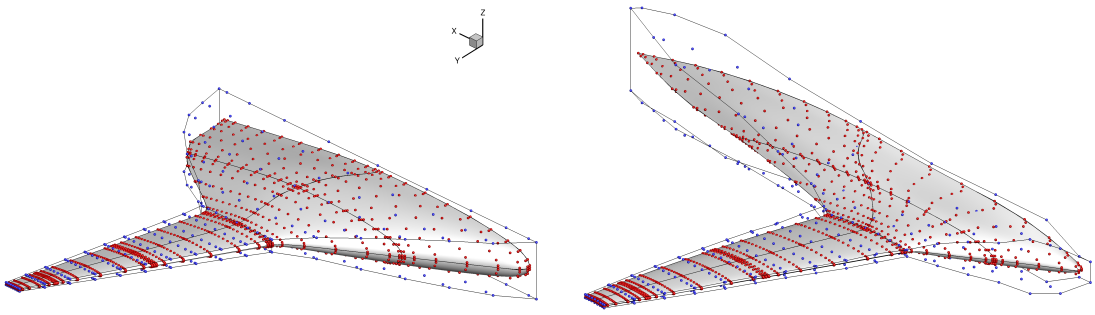

(a) Initial (b) Optimized

Figure 2.4: Planform of a BWB optimized using FFD control

[17] describe the deformation process as a two-level approach. The first level involves the control points defining the FFD volume. The second level involves the control points defining the geometry. This is illustrated by Figure 2.4. The red surface control points are embedded inside FFD volumes defined by the blue FFD control points. As the FFD points deform, the embedded surface control points move along with them, optimizing the BWB.

### Axial Deformation

The FFD approach described above was enhanced by Gagnon and Zingg with the addition of axial deformation capabilities [17]. The concept was introduced by Larazus et al. [39] and is similar in principle to FFD. First, an axial curve is placed within or outside the geometry. The points defining the object are then mapped to the nearest point along the curve. The curve is then deformed, and the coordinates of the geometry are re-evaluated based on the mapping to the axial curve.

As an example from Gagnon and Zingg [3], Figure 2.5 shows how an axial curve can be used to deform a wing. The axial curve is a B-spline curve given by Equation 2.1. In this case, it is placed at the quarter-chord, but the leading and trailing edges are also common choices. Each FFD control-point cross-section has its own local orthonormal coordinate system with its origin located on the axial curve and oriented such that the plane of each cross-section remains in line with the free-stream flow direction. The cross-sections remain "attached" to the axial curve as it is deformed through the manipulation of its B-spline control points. As before, the B-spline surface control points are embedded within the FFD volume.

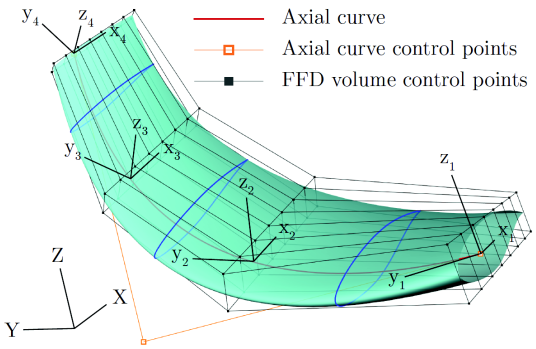


Figure 2.5: Axial deformation of an FFD volume about a generic wing (Used with permission) [3]

The complete set of design variables are defined as follows:

- Sweep: $x$-directional translation of axial control points
- Span: $y$-directional translation of axial control points
- Dihedral: $z$-directional translation of axial control points
- Twist: rotation or twist of FFD cross-sections about axial curve
- Chord: scaling FFD cross-sections about axial curve
- Section: $z$-directional translation of FFD control points in the cross-section's local coordinate system

### 2.1.4 Linear-Elasticity Mesh Movement

Aerodynamic design optimization algorithms require some method to update the computational mesh once the geometry has been modified. Mesh regeneration is often too expensive and difficult to automate, so mesh movement methods are often preferred. The mesh movement method employed in Jetstream is based on a linear-elasticity model [40]. While such models can be expensive if applied directly to the computational mesh, Jetstream makes use of the fact that the fitted B-spline mesh acts as a control mesh providing a coarser approximation to the computational mesh. By applying the linear-elastic model to the control mesh rather than the computational mesh, the mesh movement becomes much cheaper to compute while still maintaining high mesh quality [16].

The control mesh can be visualized as a solid that is elastically deformed in response to the displaced surface control points. Hexahedral cells defined by adjacent control points are assigned greater stiffness in inverse proportion to their volume to maintain the quality of the initial mesh. The system solved is defined by:

$$\boldsymbol{\mathcal{M}} = \mathbf{K}(\mathbf{b} - \mathbf{b}^{(0)}) - \mathbf{f} = 0, \tag{2.10}$$

where $\boldsymbol{\mathcal{M}}$ are the mesh residuals, $\mathbf{K}$ is the stiffness matrix, $\mathbf{b}$ and $\mathbf{b}^{(0)}$ are the updated and initial control-point coordinate column vectors, respectively, and $\mathbf{f}$ is the force vector implicitly determined from the displaced surface control points. The mesh movement can be performed in increments to improve mesh quality for large shape changes. In this case, linear interpolation between the final and initial surface control-point coordinates, $\mathbf{b}_{\text{srf}}^{(m)}$ and $\mathbf{b}_{\text{srf}}^{(0)}$, respectively, is used to determine the intermediate values

$$\mathbf{b}_{\text{srf}}^{(i)} = \frac{i}{m}\left(\mathbf{b}_{\text{srf}}^{(m)} - \mathbf{b}_{\text{srf}}^{(0)}\right) + \mathbf{b}_{\text{srf}}^{(0)}, \qquad i = 1, ..., m, \tag{2.11}$$

where $i$ is the current mesh movement increment and $m$ is the number of increments. The stiffness matrix $\mathbf{K}$ in Equation 2.10 then depends on the control-point coordinates at the previous increment. Since the original mesh fitting provides the parametric values of the grid nodes, algebraic recomputation of their coordinates in physical space is quick to perform.

## 2.2 Flow Solver

The flow solver in Jetstream is a three-dimensional multi-block structured finite-difference solver. The parallel implicit solver uses a Newton-Krylov-Schur method and is capable of solving the Euler or Reynolds-averaged Navier-Stokes (RANS) equations [41, 42]. Spatial discretization of the governing equations is performed using second-order summation-by-parts operators. Boundary and block interface conditions are enforced weakly through simultaneous approximation terms, which allow $C^1$ discontinuities in mesh lines at block interfaces. Deep convergence is efficiently achieved using an inexact-Newton phase, while globalization is provided by an approximate-Newton start-up phase. The resulting large, sparse linear system is solved using the flexible generalized minimal residual method with an approximate-Schur parallel preconditioner. The RANS equations are closed using the Spalart-Allmaras one-equation turbulence model. A scalar artificial dissipation scheme [43, 44] is used for the cases in this thesis, but matrix dissipation [45] can also be used.

## 2.3 Gradient Evaluation and Optimization Algorithm

The general optimization problem can be posed as follows:

$$\min \mathcal{J}(\mathbf{v}, \mathbf{q}, \mathbf{b}^{(m)}) \tag{2.12a}$$

$$\text{w.r.t. } \mathbf{v} \tag{2.12b}$$

$$\text{s.t. } \boldsymbol{\mathcal{M}}^{(i)}(\mathbf{A}^{(i)}(\mathbf{v}), \mathbf{b}^{(i)}, \mathbf{b}^{(i-1)}) = \boldsymbol{\mathcal{R}}(\mathbf{v}, \mathbf{q}, \mathbf{b}^{(m)}) = 0,\ i = 1, 2, ..., m \tag{2.12c}$$

where $\mathcal{J}$ is the objective function, $\mathbf{v}$ are the design variables, $\mathbf{b}^{(i)}$ are the volume control-point coordinates at mesh movement increment $i$, $m$ is the total number of mesh movement increments, $\boldsymbol{\mathcal{M}}^{(i)}$ are the mesh residuals, $\boldsymbol{\mathcal{R}}$ are the flow residuals, $\mathbf{q}$ are the flow variables, and $\mathbf{A}^{(i)}$ are the displaced surface control-point coordinates. The design variables $\mathbf{v}$ are either a subset of $\mathbf{b}^{(m)}$, if using B-spline surface geometry control, or the FFD control points, if using FFD geometry control, and may also include angle of attack. There can be additional linear and nonlinear equality and inequality constraints.

### 2.3.1 Gradient Evaluation

Gradients are calculated using the discrete-adjoint method at a cost virtually independent of the number of design variables. While it has been shown that gradient-based multistart or hybrid algorithms can be used for multimodal problems [46], this approach is not taken here. Therefore, the minima achieved are local minima, and may or may not be global minima. To perform the constrained optimization, the Lagrangian function is introduced:

$$\mathcal{L} \equiv \mathcal{J} + \boldsymbol{\Lambda}^T \mathbf{c} \tag{2.13}$$

where $\boldsymbol{\Lambda}^T = \{\boldsymbol{\lambda}^{(i)}, \boldsymbol{\psi}\}_{i=1}^m$ are the Lagrange multipliers, also called the adjoint variables. $\{\boldsymbol{\lambda}^{(i)}\}_{i=1}^m$ and $\boldsymbol{\psi}$ are mesh and flow adjoint variables, respectively. For optimality, the Karush-Kuhn-Tucker (KKT) conditions must be satisfied [47]. Once the mesh movement and flow solution have been computed, the resulting flow and mesh adjoint equations must be solved. The flow Jacobian matrix is formed by linearizing its components, including the viscous and inviscid fluxes, the artificial dissipation, the turbulence model, and the boundary conditions. The flow adjoint system is solved using a modified, flexible version of GCROT [48, 49, 50], and the mesh adjoint system is solved using a preconditioned conjugate-gradient method. The final KKT condition gives rise to the objective gradient

calculation:

$$\frac{\partial \mathcal{L}}{\partial \mathbf{v}} = \frac{\partial \mathcal{J}}{\partial \mathbf{v}} + \sum_{i=1}^{m} \left( \boldsymbol{\lambda}^{(i)T} \frac{\partial \boldsymbol{\mathcal{M}}^{(i)}}{\partial \mathbf{A}^{(i)}} \frac{\partial \mathbf{A}^{(i)}}{\partial \mathbf{A}^{(m)}} \frac{\partial \mathbf{A}^{(m)}}{\partial \mathbf{v}} \right) + \boldsymbol{\psi}^{T} \frac{\partial \boldsymbol{\mathcal{R}}}{\partial \mathbf{v}}. \tag{2.14}$$

### 2.3.2 SNOPT

Once the gradients are computed, they are passed to SNOPT (Sparse Nonlinear OPTimizer) [51], a gradient-based optimization algorithm. It can handle both linear and nonlinear constraints, satisfying linear constraints exactly. SNOPT applies a sparse sequential quadratic programming algorithm that approximates the Hessian using a limited-memory quasi-Newton method.

# Chapter 3

# Results

## 3.1 Case 1: Symmetric Optimization of NACA 0012 Airfoil in Inviscid Transonic Flow

### 3.1.1 Optimization Problem

The optimization problem is the drag minimization of a modified NACA 0012 airfoil in inviscid, transonic flow. The freestream Mach number is 0.85, and the angle of attack is fixed at 0°, based on Vassberg et al. [25] The design variables are the $z$-coordinates of the B-spline surface or FFD control points. The thickness is constrained to be greater than or equal to the initial airfoil thickness along the entire chord. Linear symmetry constraints maintain a symmetric airfoil. The problem can be summarized as

$$\begin{aligned} &\text{minimize } C_d \\ &\text{w.r.t. } z \\ &\text{subject to } |z| \geq |z_{\text{baseline}}|, \end{aligned}$$

where $C_d$ is the drag coefficient, $z$ is the $z$-coordinate of a node on the optimized airfoil, and $z_{\text{baseline}}$ is the $z$-coordinate of the corresponding node on the initial geometry.

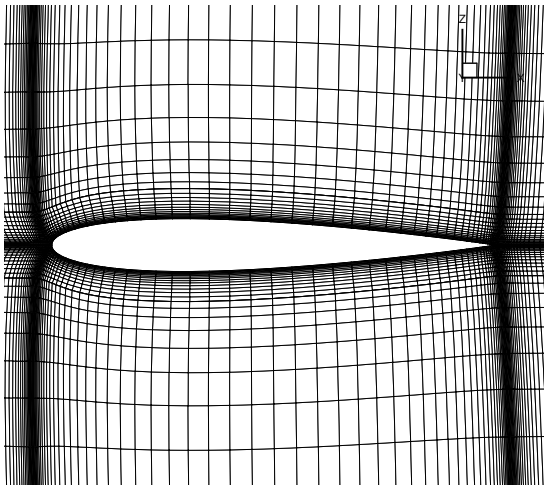

Figure 3.1: Case 1 - Coarse grid for modified NACA 0012 airfoil

### 3.1.2 Initial Geometry

The initial airfoil is a NACA 0012 modified to have a zero-thickness trailing edge. The airfoil is defined by

$$z_{\text{baseline}} = \pm 0.6(0.2969\sqrt{x} - 0.1260x - 0.3516x^2 + 0.2843x^3 - 0.1036x^4),\ x \in [0, 1]. \quad (3.1)$$

The modification is to the $x^4$ term coefficient, to allow for a zero-thickness trailing edge.

### 3.1.3 Grid

A structured H-topology grid around a flat plate of unit chord is inflated using the mesh movement methodology to fit the NACA 0012 section. Two surface patches define the geometry, one on the top and one on the bottom. To establish mesh convergence, four grid levels are considered. Starting with the coarsest grid, refined grids are obtained by parametric refinement, which sequentially doubles the number of nodes in each direction and preserves the hyperbolic nodal distribution of the coarsest grid. The coarse grid is displayed in Figure 3.1. Since Jetstream was developed for 3D optimization, the airfoil grids are extruded in the spanwise direction. Ten nodes are located along the unit span. Key grid spacing parameters in terms of chord units c are recorded in Table 3.1. Flow analysis is performed for the initial geometry fitted with 52 streamwise control points per surface, and the drag coefficient values are recorded in Table 3.2. Between the fine and superfine grids, a difference of less than 0.2 drag counts is seen. The coarse grid is

Table 3.1: Case 1 - Grid parameters for NACA 0012 airfoil grid study

| **Grid** | **Nodes (2D)** | **Off-wall Spacing (c)** | **Leading-Edge Spacing (c)** | **Trailing-Edge Spacing (c)** |
|---|---|---|---|---|
| Coarse | 15,390 | 0.0012 | 0.0012 | 0.0012 |
| Medium | 58,986 | 0.00058 | 0.00058 | 0.00058 |
| Fine | 230,850 | 0.00028 | 0.00028 | 0.00028 |
| Superfine | 921,348 | 0.00014 | 0.00014 | 0.00014 |

Table 3.2: Case 1 - Results of grid study for initial NACA 0012 airfoil

| **Grid Level** | **Nodes (2D)** | **$C_d$ (Counts)** |
|---|---|---|
| Coarse | 15,390 | 453.16 |
| Medium | 58,986 | 457.33 |
| Fine | 230,850 | 458.05 |
| Superfine | 921,348 | 458.20 |

used for optimization.

### 3.1.4 Optimization Results

The results presented herein are obtained from analyses on the coarse mesh level, unless otherwise indicated. Although fine-mesh results would be preferred, mesh refinement of the optimized geometries changes the physics of the flow significantly, in such a way that comparisons between the two geometry control methods becomes no longer reliable at the fine mesh level. This will be demonstrated more precisely later in the section. It is also worth mentioning that setting up the optimizations with both geometry control methods is of similar difficulty for each; no significant advantage for problem setup is offered by either method for this case. The initial design variables for both cases with 50 design variable are displayed in Figure 3.2.

Mach number and entropy contours are displayed in Figures 3.3 and 3.4, respectively, for the initial and optimized geometries using 50 B-spline design variables on the upper

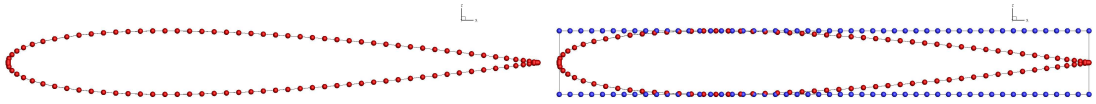

(a) Initial B-spline optimization setup (b) Initial FFD optimization setup

Figure 3.2: Case 1 - Initial 50 chordwise geometric design variables per surface for B-spline surface (red points) and FFD (blue points) control

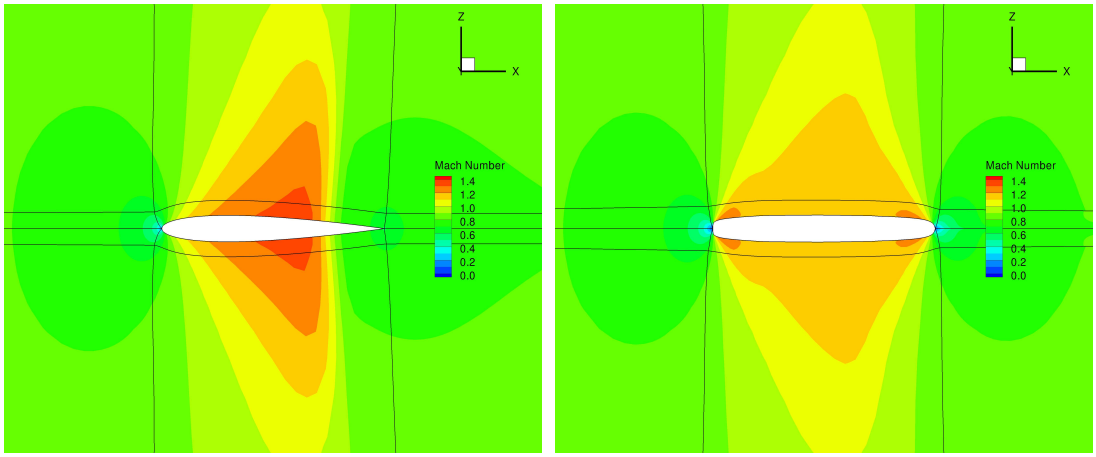


(a) Initial (b) Final

Figure 3.3: Case 1 - Comparison of Mach contours for initial NACA 0012 airfoil and final optimized shape with 50 B-spline surface design variables

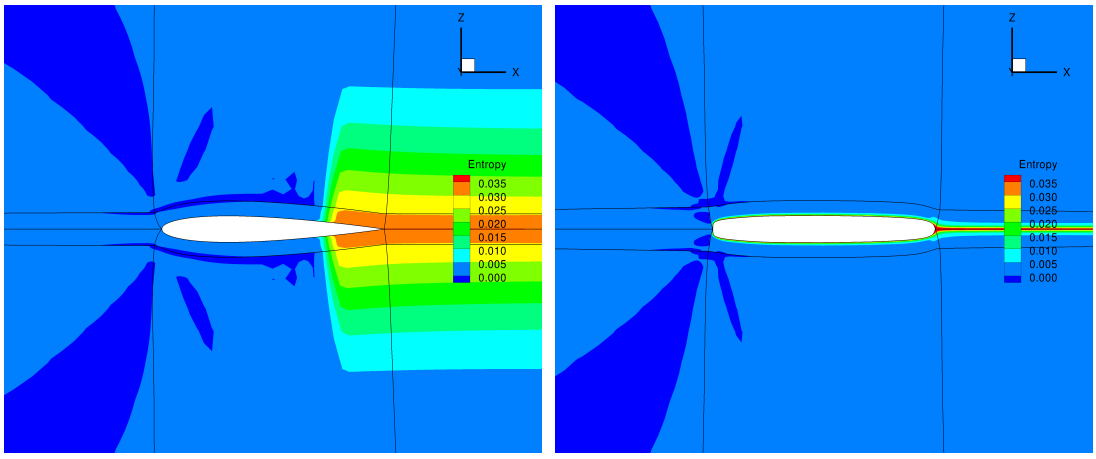


(a) Initial (b) Final

Figure 3.4: Case 1 - Comparison of entropy contours for initial NACA 0012 airfoil and final optimized shape with 50 B-spline surface design variables

and lower surfaces. Strong shocks extending far into the flow field are evident on the initial geometry. Due to the thickness constraint, the optimizer thickens the airfoil, creating a relatively flat surface that delays the pressure recovery. Weaker shocks, which do not extend as far into the flow field, occur near the trailing edge of the optimized airfoil. The optimized geometry is quite blunt, since the optimizer is exploiting the fact that the Euler equations cannot correctly model the physics of flow separation, but it is worth noting that RANS analysis would likely show significant separation. The design problem is meant to be more of a challenging academic problem than a practical one.

Optimizations are conducted to investigate the effect of design space dimensionality. The number of design variables for each surface ranges from 10 to 50. The initial suite of FFD optimizations spanning the range of design variables is run with a uniform distribution of FFD control points in the chordwise direction. 52 surface control points defining each of the upper and lower surfaces are embedded in the FFD volumes. An additional FFD optimization is run with a cosine distribution of 50 design variables in the chordwise direction, clustering FFD control points toward the leading and trailing edges. The distribution of FFD control points $\mathbf{d}$, normalized by the chordwise length of the FFD cross-section, is given by

$$\mathbf{d} = \frac{\cos(\mathbf{u}) + 1}{2} \tag{3.2}$$

where $\mathbf{u} = [\pi, \pi - (1)\frac{\pi}{n-1}, ..., \pi - (n-2)\frac{\pi}{n-1}, 0]$, and $n$ is the desired number of FFD control points in the chordwise direction, which is 50 in this case. Figure 3.5 plots airfoil surfaces and corresponding pressure coefficients for the initial and final geometries with 10 and 50 design variables on each surface, evaluated on the coarse mesh. With more design variables, the optimizer has more freedom to create slightly blunter leading and trailing edges. The suction peak becomes more abrupt; the shock is weakened and pushed slightly further downstream. The drag coefficient of the final geometries from both geometry control methods is plotted against the number of design variables in Figure 3.6. For the same number of design variables, B-spline surface control consistently gives lower drag. The surface control-point clustering in the leading- and trailing-edge regions provide a significant advantage over the uniformly distributed FFD control points, since highly localized control in these regions is important for this case. However, clustering the FFD control points at the leading and trailing edges gives improved drag reduction, as shown in Figure 3.6. The case with 50 B-spline surface design variables now only outperforms FFD by about 2.5 counts, and further clustering would likely reduce this difference even

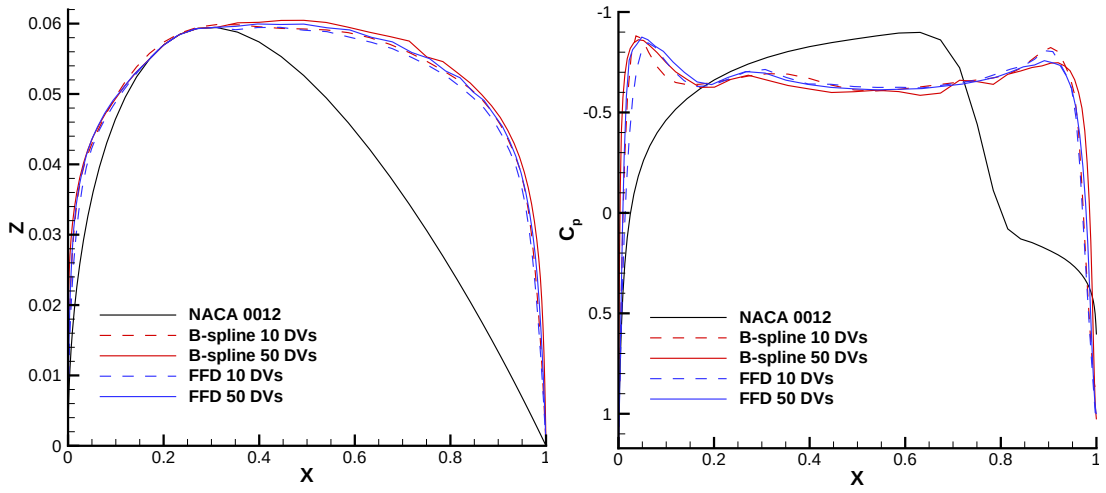


(a) Airfoils

(b) $C_p$ curves

Figure 3.5: Case 1 - Comparison of initial and final airfoil shapes and corresponding pressure distributions (uniform FFD distribution results shown)

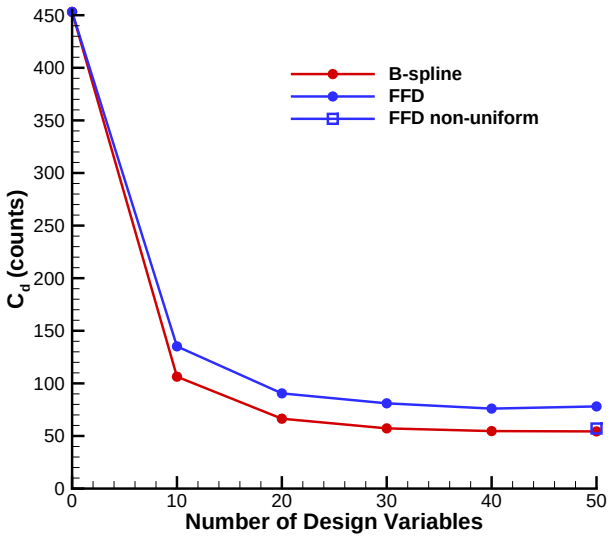


Figure 3.6: Case 1 - Drag comparison of final geometries

more. The lowest drag is obtained using 50 B-spline design variables per surface: 54.55 drag counts, an 88% reduction from the initial geometry.

Figure 3.7 shows the convergence history for 10 and 50 design variables. Optimality, which is a measure of convergence of the optimization to a local minimum, has a convergence tolerance set at $1\times10^{-7}$. As the number of design variables increases, the optimizer has a more difficult time reducing optimality for both geometry control methods. The plots of the merit function, which is the objective function plus penalty terms

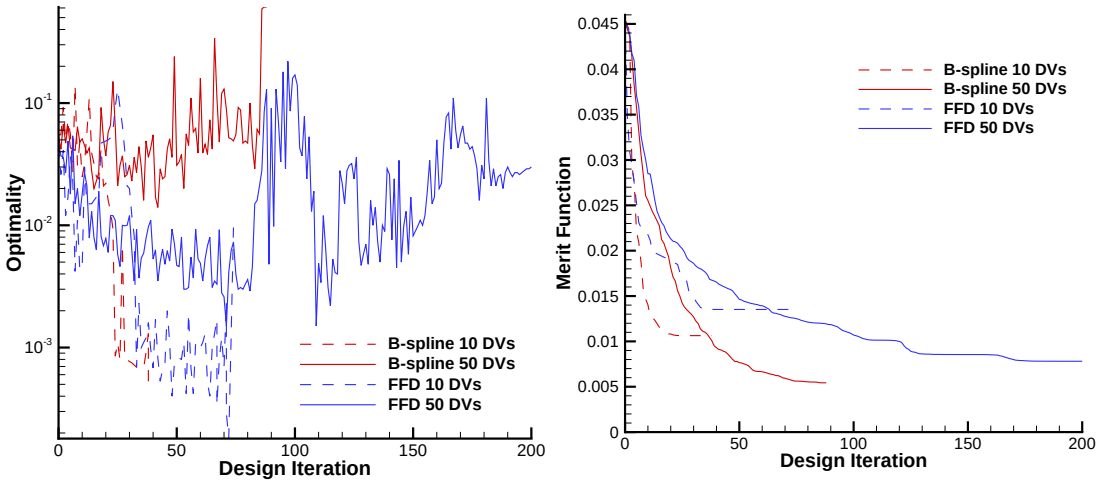


(a) Optimality

(b) Merit function

Figure 3.7: Case 1 - Typical convergence histories for NACA 0012 airfoil optimization (uniform FFD distribution results shown)

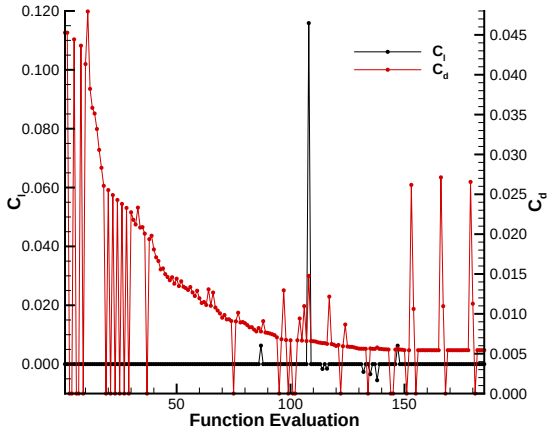


Figure 3.8: Case 1 - Functional history during 50 B-spline design variable optimization

for nonlinear constraint violations, show that drag is still reduced over the course of the optimizations. In this case, the merit function is equal to the objective because there are no nonlinear constraints. B-spline surface control reduces the drag at a faster rate, but the difference can likely be reduced by adjusting design variable scaling.

To further investigate the difficulties in converging optimality, the optimization histories over function evaluations are examined. For example, $C_l$ and $C_d$ are plotted during the 50 B-spline design variable optimization in Figure 3.8. The data points giving zero drag correspond to failed function evaluations, most of which are flow solves that failed to converge. What is suprising from this plot is the presence of flow solutions giving

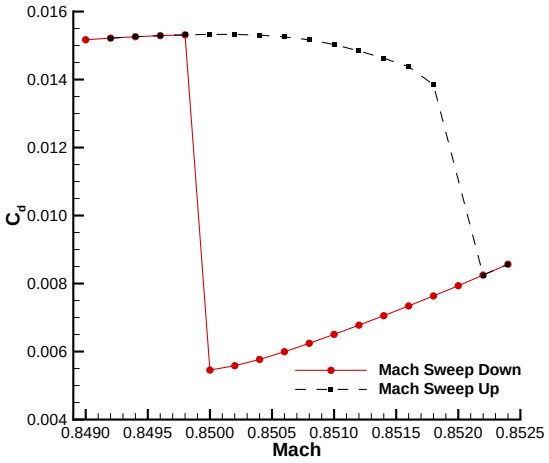


Figure 3.9: Case 1 - Drag coefficient hysteresis over Mach number

non-zero lift, even though the airfoils are consistently symmetric at zero angle of attack. These lifting solutions suggest the presence of non-unique solutions in the design space. Lifting solutions give higher drag values that the optimizer does not expect from the gradient information. Such instances are detrimental to the optimization convergence. The problem worsens with more design variables, due to an increased ability to find non-unique solutions as the airfoil becomes increasingly bluff.

To demonstrate that these lifting solutions are in fact due to non-uniqueness, flow analyses were conducted for the final geometry from the optimization with 50 B-spline design variables, sweeping down from an initial Mach number of 0.8524 to 0.8490, and then back up again. Each flow solution was initialized using the previous converged solution. Figure 3.9 shows that hysteresis behaviour is observed. Non-unique solutions occur over a small range of Mach numbers, and in fact, the nominal condition of Mach 0.85 is right at the lower bound of the non-unique range.

The presence of non-unique solutions may be due to the fact that the Euler equations are ill-suited for such bluff bodies. As previously stated, RANS analysis would likely give considerable flow separation, and unsteady analysis would perhaps give unsteady flow features [27]. Hence, forcing the flow to remain tangent to the highly "blunt" trailing edge is unphysical, and this may be contributing to the ill-posedness of the problem.

To examine the lifting solutions further, the pressure distribution from the upper branch $M = 0.85$ solution of Figure 3.9 is displayed in Figure 3.10. A double shock is observed on the lower surface and a single shock on the upper surface, consistent with the double shocks observed by Jameson et al. [26], who analyzed similar bluff airfoils under

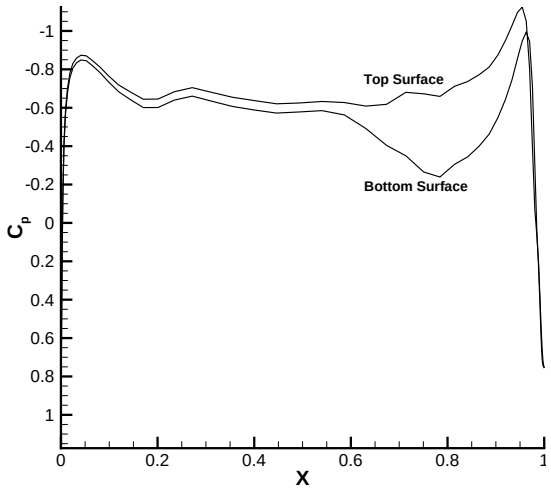


Figure 3.10: Case 1 - Pressure coefficient for final geometry from 50 B-spline design variable optimization

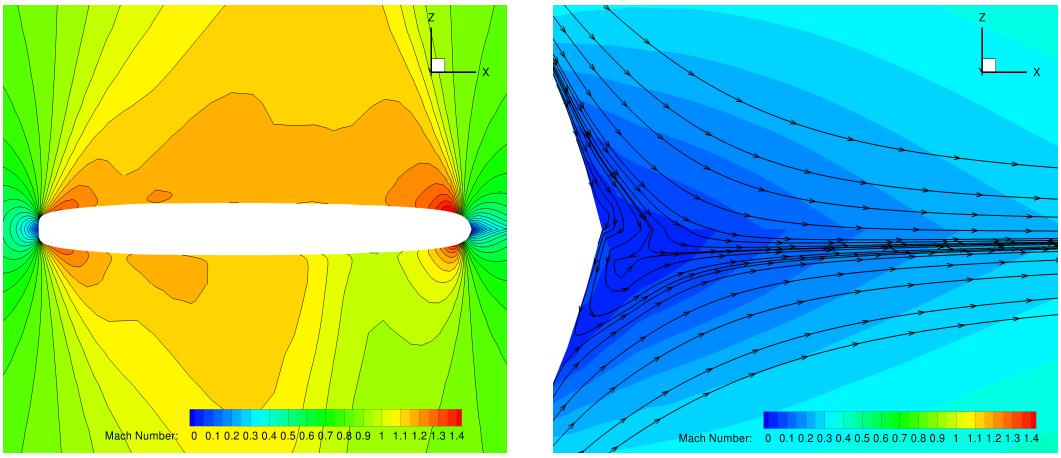


(a) Mach contours about airfoil

(b) Streamlines in trailing-edge region

Figure 3.11: Case 1 - Mach contours and streamlines for final geometry from 50 B-spline design variable optimization, from upper branch of Mach hysteresis loop

similar flow conditions. Mach contours and streamlines are displayed in Figure 3.11, with a zoomed view of the trailing-edge region. Recirculating flow is observed. Examination of other lifting solutions shows similar flow features.

Now that it is understood that the Euler equations are ill-suited for the geometries resulting from the optimizations, the reasoning for presenting coarse mesh results, as opposed to fine mesh results, can be demonstrated. A mesh refinement study was conducted for the 50 B-spline design variable geometry. Initializing the flow solutions on the medium and fine meshes using free-stream conditions resulted in lifting solutions, so

Table 3.3: Case 1 - Results of grid study for optimized airfoil using 50 B-spline surface design variables

| Grid Level | Nodes (2D) | $C_D$ (Counts) |
|---|---|---|
| Coarse | 15,390 | 54.55 |
| Medium | 58,986 | 37.71 |
| Fine | 230,850 | 63.29 |

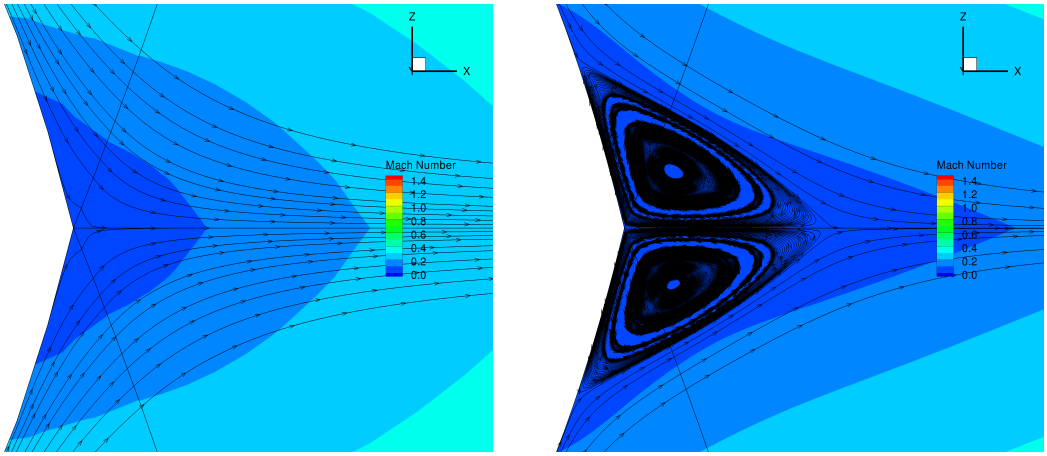


(a) Coarse mesh (b) Fine mesh

Figure 3.12: Case 1 - Mach contours and streamlines for final geometry from 50 B-spline design variable optimization, from lower branch of Mach hysteresis loop

the warm-starting approach used to produce Figure 3.9 had to be employed to give the zero-lift solution. A converged solution could not be obtained on the superfine mesh. The results are shown in Table 3.3.

Given the significant decrease in drag between the coarse and medium meshes, the subsequent large increase in drag between the medium and fine mesh is unexpected. Examination of the flow fields, as shown in Figure 3.12, shows a significant change in the flow physics in the trailing-edge region with refinement. On the coarse and medium meshes (the medium mesh solution is omitted for brevity), the streamlines show the expected well-behaved flow. On the fine mesh, however, a recirulation zone appears while still maintaining flow tangency to the surface, giving the increased drag. Just as the flow solver seems more prone to converging to lifting solutions as the grid is refined, refinement also gives a recirculation zone where the Euler equations are most

ill-suited. Unfortunately, this behaviour is also observed on the medium mesh for some other geometries. Since the appearance of such recirculation increases the drag for a given geometry unpredictably, coarse mesh results were deemed more appropriate for the earlier discussions in this section. It is likely that this behaviour was not observed for previous geometries generated using Jetstream for this problem due to the comparatively coarse off-wall spacings of the meshes used in these other investigations [29, 30].

To sum up the results for this case, the airfoil with lowest drag is obtained by optimizing with 50 B-spline surface design variables per surface. A $C_d$ of 54.55 drag counts is computed on the coarse mesh. The two geometry control methods perform equally well, however, when appropriate control-point clustering is employed. The presence of non-unique solutions in the design space inhibits the optimizations from demonstrating the full potential of each control method, so additional investigations with other cases are necessary.

## 3.2 Case 2: Optimization of RAE 2822 Airfoil in Viscous Transonic Flow

### 3.2.1 Optimization Problem

The optimization problem is the drag minimization of the RAE 2822 airfoil in viscous, transonic flow. The freestream Mach number is 0.734, and the Reynolds number is 6.5 million. The design variables are the $z$-coordinates of the B-spline surface or FFD control points, as well as the angle of attack. The lift coefficient is constrained to 0.824 and the moment coefficient about the quarter-chord must be no less than -0.092. The minimum airfoil area is the initial airfoil area. Though not required by the ADODG test description, a minimum thickness constraint of 25% of the initial thickness is enforced to maintain a realistic design and prevent control point cross-over. The problem can be summarized as

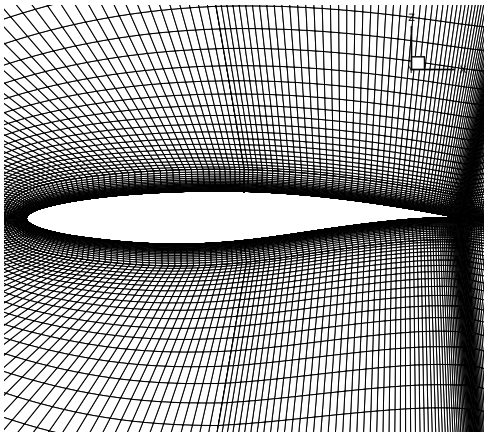

Figure 3.13: Case 2 - Coarse grid around RAE 2822 airfoil used for optimizations

$$\begin{aligned} &\text{minimize } C_d \\ &\text{w.r.t. } z,\ \alpha \\ &\text{subject to } C_l = 0.824 \\ &\qquad\qquad C_m \geq -0.092 \\ &\qquad\qquad A \geq A_{\text{baseline}} \end{aligned}$$

where $C_d$, $C_l$, and $C_m$ are the drag, lift, and moment coefficients, respectively, and $A$ and $A_{\text{baseline}}$ are the optimized and initial airfoil areas, respectively.

### 3.2.2 Initial Geometry

The initial geometry is the RAE 2822 airfoil. The coordinates are obtained from the UIUC Airfoil Coordinates Database.

### 3.2.3 Grid

A C-topology grid is used for this case, and the grid used for the optimization studies is displayed in Figure 3.13. To establish grid convergence, the optimization grid was repeatedly refined by a factor of two in each direction, giving the grid family with parameters shown in terms of chord units in Table 3.4. The locations of the new nodes added during refinement preserve the hyperbolic nodal distribution, giving a consistent grid family.

Table 3.4: Case 2 - Grid parameters for RAE 2822 airfoil grid study

| **Grid** | **Nodes (2D)** | **Off-wall Spacing (c)** | **Leading-Edge Spacing (c)** | **Trailing-Edge Spacing (c)** |
|---|---|---|---|---|
| Coarse | 47,824 | $3.7\times10^{-6}$ | $1\times10^{-3}$ | $1\times10^{-3}$ |
| Medium | 187,792 | $1.8\times10^{-6}$ | $5\times10^{-4}$ | $5\times10^{-4}$ |
| Fine | 748,064 | $8.7\times10^{-7}$ | $2.5\times10^{-4}$ | $2.5\times10^{-4}$ |
| Superfine | 3,016,832 | $4.3\times10^{-7}$ | $1.25\times10^{-4}$ | $1.25\times10^{-4}$ |
| Finest | 12,067,328 | $2.1\times10^{-7}$ | $6.25\times10^{-5}$ | $6.25\times10^{-5}$ |

Table 3.5: Case 2 - Results of grid study for initial RAE 2822 airfoil

| **Grid Level** | $\mathbf{y^+}$ | $\mathbf{C_l}$ | $\mathbf{C_d}$ **(Counts)** | $\mathbf{C_m}$ |
|---|---|---|---|---|
| Coarse | 0.71 | 0.8240 | 234.44 | -0.0908 |
| Medium | 0.32 | 0.8439 | 228.41 | -0.0932 |
| Fine | 0.15 | 0.8501 | 229.14 | -0.0944 |
| Superfine | 0.076 | 0.8519 | 229.61 | -0.0947 |
| Finest | 0.038 | 0.8524 | 229.69 | -0.0948 |

On the optimization grid, an angle of attack of 3.119° satisfies the desired $C_l$ of 0.824. Coefficients of drag, lift, and moment, as well as average $y^+$, are reported in Table 3.5. The desired drag resolution of 0.1 counts is achieved between the two finest grid levels, but lift is not within $0.1\times10^{-4}$.

To evaluate the accuracy of the finest grid level, numerical results were obtained to compare to the commonly referenced experimental results for the RAE 2822 - Case 9 [52]. The flow conditions for the analysis were set to match the experimental flow conditions: a Mach number of 0.73, Reynolds number of 6.5 million, and corrected wind tunnel angle of attack of 2.79°. The experimental results give a normal force coefficient $C_n$ of 0.803, a $C_d$ of 0.0168, and a $C_m$ of -0.099. The analysis on the finest grid level gives a $C_n$ of 0.802, a $C_d$ of 0.0167, and a $C_m$ of -0.091. In addition, pressure coefficients are compared in Figure 3.14. The computed results agree well with experiment.

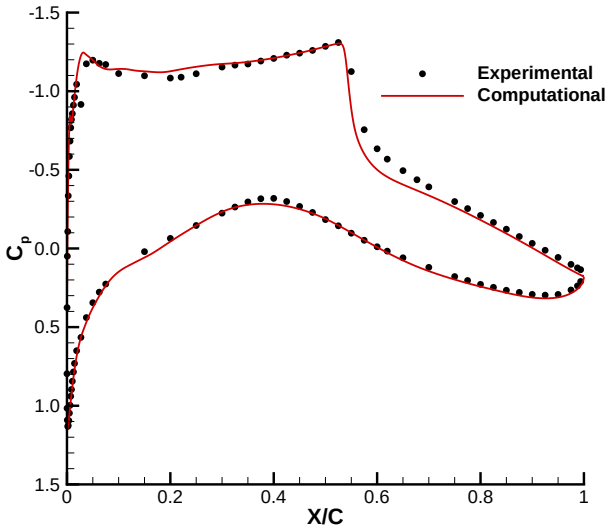


Figure 3.14: Case 2 - Comparison of experimental and computed pressure coefficient on finest grid level

### 3.2.4 Geometry Control Setup

Both geometry control methods are straightforward to set up for this case. Since two patches are used to define each of the top and bottom surfaces, a linear constraint is used with B-spline surface control to maintain $C^1$ continuity at the patch interface. Mathematically maintaining continuity at the interface using FFD control would require a nonlinear constraint, since it is the FFD control points rather than the surface control points that are the design variables. However, the FFD control-point spacing in the region of the interface typically exceeds the surface control-point spacing at the interface. This tends to smooth the changes produced by the FFD and yield smaller $C^1$ discontinuities. Hence, a nonlinear continuity constraint is not used for the FFD optimizations.

A more significant difference comes from the need to fix the leading- and trailing-edge surface control points in space. With B-spline surface control, this is trivial, and just involves setting the degrees of freedom of these control points to zero. With FFD control, since the surface control points of interest lie in the middle of the leading- and trailing-edge faces of the FFD volume, the leading- and trailing-edge FFD control points have to be constrained to move symmetrically about the embedded points. This highlights one of the disadvantages of FFD, in that its lack of direct surface control makes constraining surface points more difficult. In this case, the approach of symmetry constraints is easy to implement, but as shall be seen in Section 3.4.4, a more general approach is more

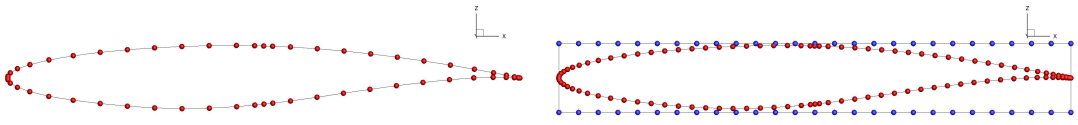

(a) Initial B-spline optimization setup (b) Initial FFD optimization setup

Figure 3.15: Case 2 - Initial geometric design variables for B-spline surface (red points) and FFD (blue points) control

involved. In addition, symmetry constraints at the leading- and trailing-edges can limit camber changes in these regions.

### 3.2.5 Optimization Results

To examine the effect of design space dimensionality, optimizations with B-spline surface control were conducted with from 6 to 36 chordwise design variables on each of the top and bottom surfaces, and optimizations with FFD control were conducted with from 5 to 37 design variables on each of the top and bottom of the FFD volume. For the FFD cases, 53 chordwise surface control points parameterize each of the top and bottom surfaces of the airfoil. Examples of the initial design variables for both cases are displayed in Figure 3.15. The angle of attack is also a design variable.

Lift, drag, and moment coefficient values are plotted in Figure 3.16, along with the angle of attack for the final geometries evaluated on the optimization grid. The initial suite of FFD optimizations spanning the range of design variables is run with a uniform distribution of FFD control points in the chordwise direction. An additional FFD optimization is run with a cosine distribution of 11 design variables in the chordwise direction. Although monotonic drag reduction is observed when the number of design variables is increased for a relatively low number of design variables, the drag reduction performance degrades for higher numbers of design variables. Noticeable differences in the final geometries are also evident, as shown in Figure 3.17. The case with 16 B-spline surface design variables gave the lowest drag among the B-spline control optimizations, and the case with 11 non-uniformly distributed FFD design variables gave the lowest drag among the FFD control optimizations. The non-uniform distribution provides greater geometry control at the leading and trailing edges, leading to greater drag reduction than the uniform distribution and very similar results to the B-spline surface optimizations with 10 and 12 design variables. The cases with 26 B-spline surface and 27 FFD design

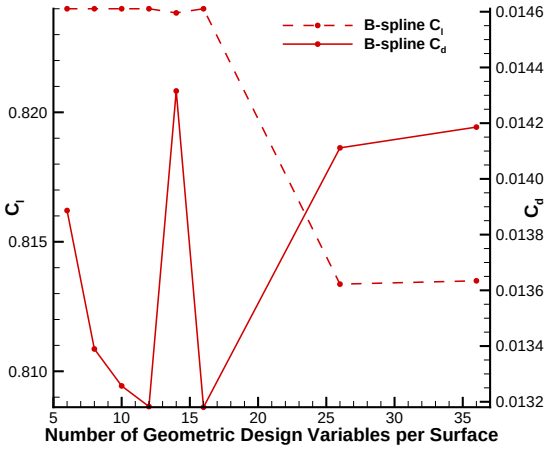


(a) B-spline control $C_l$ and $C_d$ results

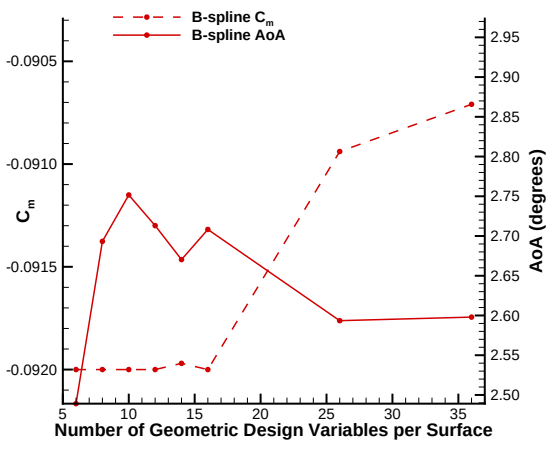


(b) B-spline control $C_m$ and $\alpha$ results

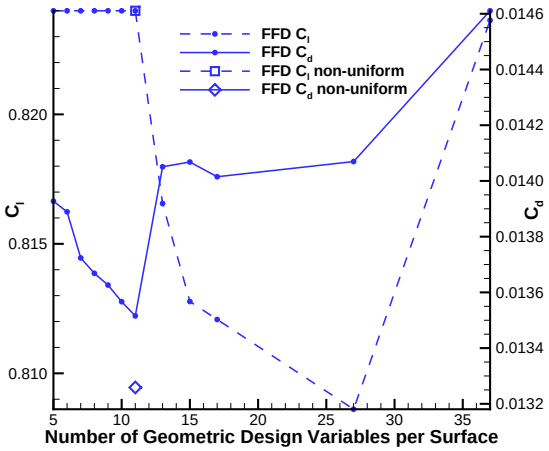


(c) FFD control $C_l$ and $C_d$ results

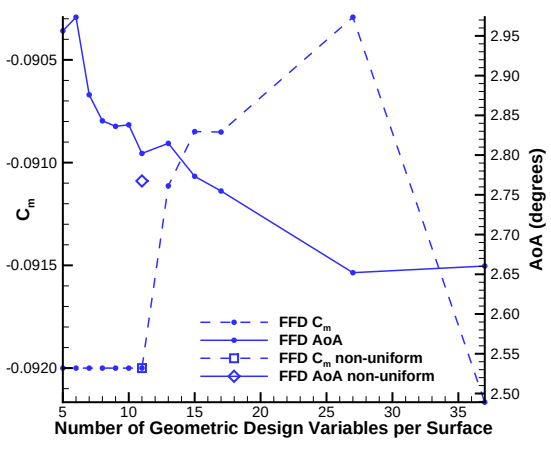


(d) FFD control $C_m$ and $\alpha$ results

Figure 3.16: Case 2 - Coarse-mesh optimization functionals and angle of attack

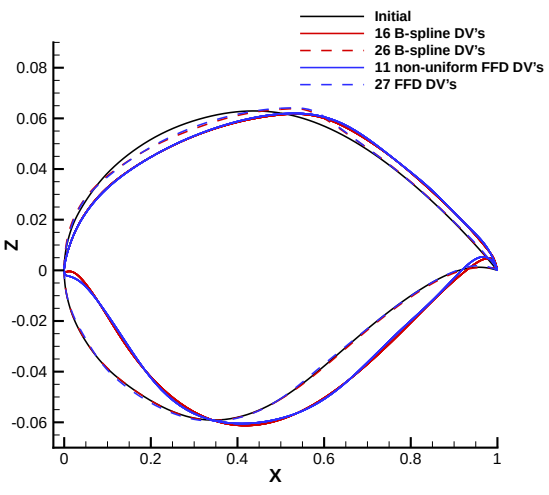


(e) Airfoil shapes

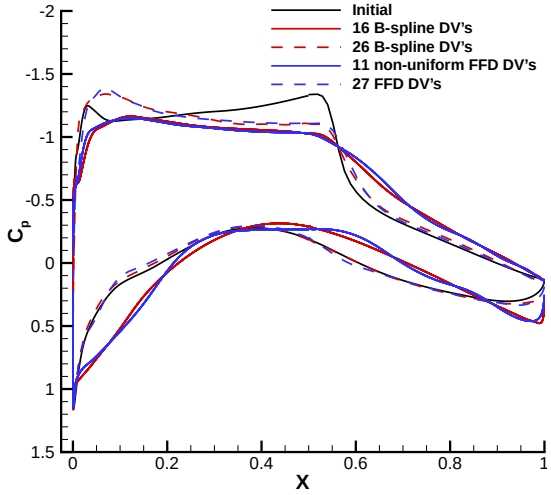


(f) $C_p$ curves

Figure 3.17: Case 2 - Airfoil shapes and pressure coefficients

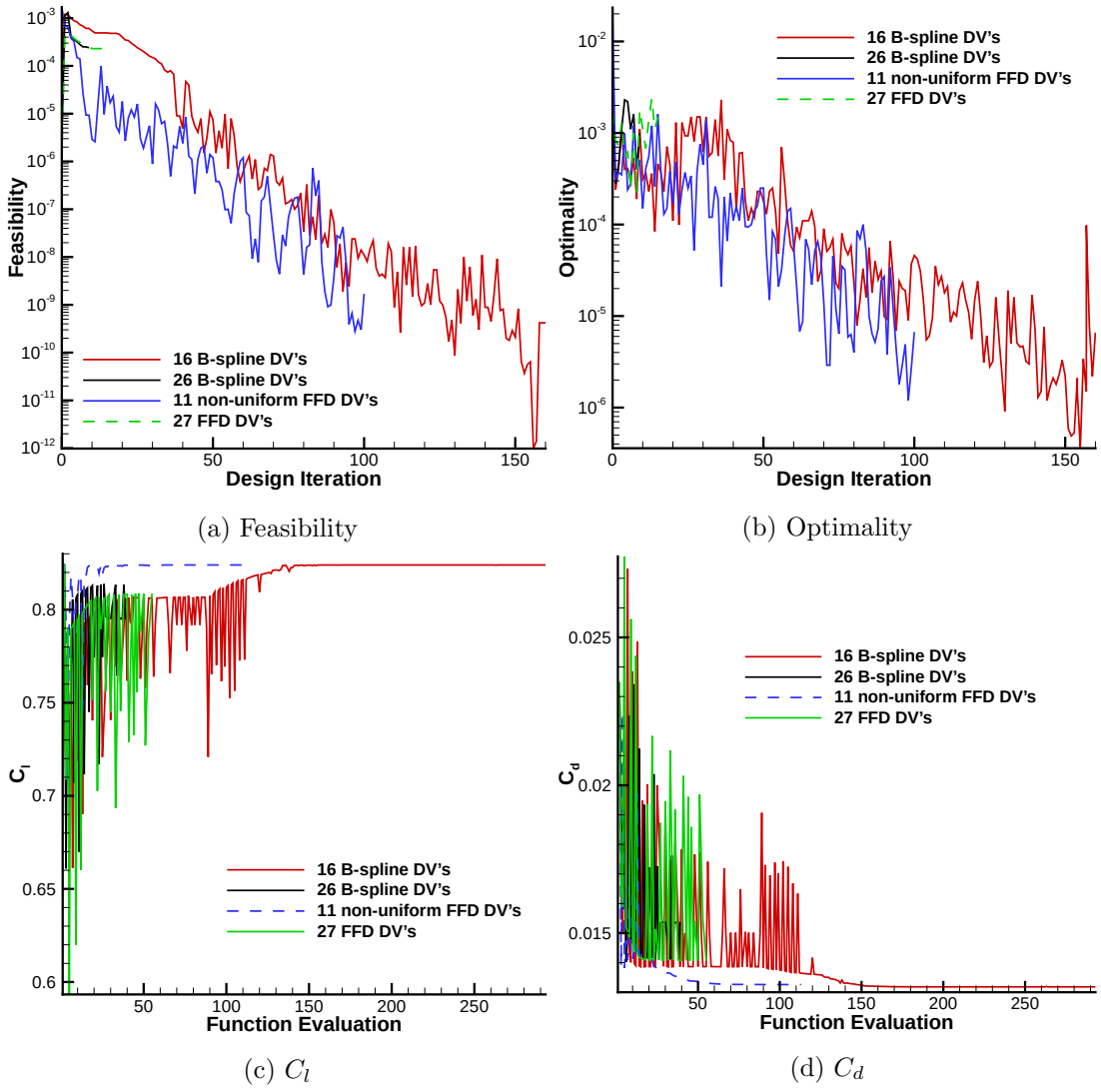


(a) Feasibility

(b) Optimality

(c) $C_l$

(d) $C_d$

Figure 3.18: Case 2 - Convergence histories

variables did not perform well. The superior geometries exhibit small leading-edge radii and highly cambered trailing edges.

Figure 3.18 compares the optimization convergence histories of the B-spline surface control cases with 16 and 26 design variables and FFD control cases with 11 non-uniformly distributed and 27 uniformly distributed design variables. Figures 3.18(a) and 3.18(b) plot feasibilility and optimality as a function of design iterations. The optimality and feasibility tolerances are set at $1\times10^{-7}$ and $1\times10^{-6}$, respectively. The cases with 16 B-spline surface and 11 FFD design variables show far superior optimization covergence. The cases with 26 B-spline surface and 27 FFD design variables ran very few iterations and do not satisfy the $C_l$ constraint. Figures 3.18(c) and 3.18(d) display lift and drag

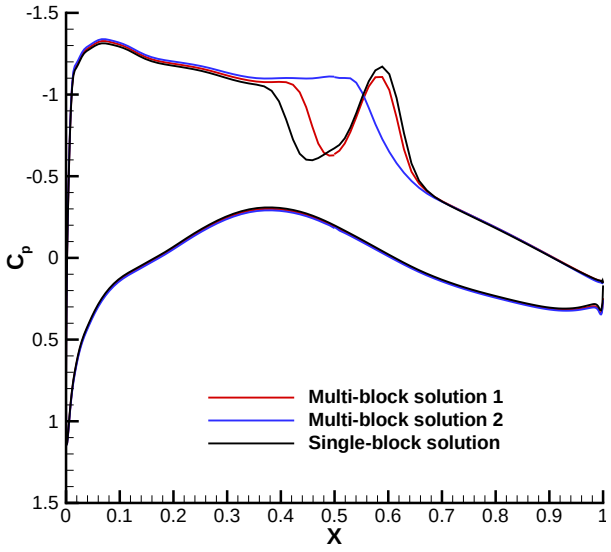


Figure 3.19: Case 2 - Pressure distributions for non-unique solutions

coefficient histories versus function evaluations. While the cases with 16 B-spline surface and 11 FFD design variables exhibit drag spikes early on in the optimization, these spikes disappear and monotonic drag reduction is observed. In contrast, the cases with 26 B-spline surface and 27 FFD design variables continue to periodically produce designs with dramatic drag increases and lift decreases, and terminate early.

The geometry at iteration 36 from the case with 26 surface design variables was re-analyzed using three different convergence paths to steady state at the design angle of attack of 2.593°. Two distinct fully converged solutions were obtained, giving $(C_l, C_d)$ pairs of (0.7830, 0.01632) and (0.8133, 0.01411). Unsteady RANS analysis demonstrated that the two steady solutions are physically stable. The pressure distributions are displayed in Figure 3.19. Note that the single-block solution shown will be discussed later. Interestingly, the discrepancies in the solutions are quite localized. The double pressure recovery features are consistent with curves observed for this case by LeDoux et al. [34]

The presence of non-unique solutions in the design space explains the poor convergence of some of the optimizations. Analyses of other geometries using the different convergence paths were conducted, and while non-unique solutions were not always observed, they were found to be common. Gradient-based optimization does not work well with design spaces that are not smooth, since search directions provided by gradient calculations can lead to unexpected spikes in the design space. For reasons not fully understood, the combination of geometries produced by the optimizations with these flow conditions yield ill-posed problems. It also appears that the occurrence of non-unique

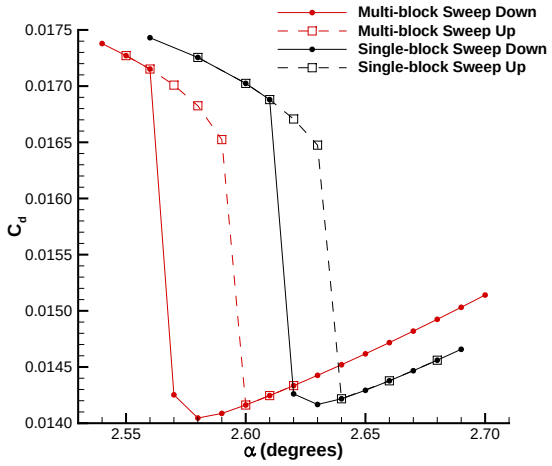


Figure 3.20: Case 2 - Drag coefficient hysteresis over angle of attack for both multi-block and single block grids

solutions is a greater problem with more design variables, since the increased geometric flexibility gives more freedom to fall into these undesired regions in the design space. While one would expect that the cases with more design variables should have the geometric flexibility to produce the geometries resembling the fewer design variable geometries, it seems that with more design variables and occurrences of non-unique solutions, the optimizer is more prone to get stuck.

The grid for geometry number 36 from the case with 26 surface design variables was converted from a multi-block grid to single-block grid. Analysis of the single-block grid in Jetstream with different convergence paths all gave a single solution, with lift and drag coefficient values of 0.7570 and 0.01711, respectively. In addition, this single solution is distinct from both multi-block solutions, as shown in the pressure coefficient plots of Figure 3.19. A double pressure recovery is observed. Several other geometries that gave non-unique solutions with multi-block meshes were analyzed with a single-block mesh, and all gave unique solutions. To more thoroughly verify whether the non-uniqueness is triggered by the treatment of block interfaces, a plot analogous to Figure 3.9 was constructed by sweeping through a range of angles of attack while initializing each flow solution using the previous converged solution. This was done on both the multi-block and single block grids, and the results are shown in Figure 3.20. The plots show that both grids yield non-unique solutions, just over different ranges of angles of attack, which is why only a single solution at 2.593° is found for Figure 3.19 using the single-block grid. This demonstrates that the treatment of the block interfaces is not the cause of the

Table 3.6: Case 2 - Results of grid study for optimized RAE 2822 airfoil using 17 design variables per surface

| **Grid Level** | $\mathbf{y^+}$ | $\mathbf{C_l}$ | $\mathbf{C_d}$ **(Counts)** | $\mathbf{C_m}$ |
|---|---|---|---|---|
| Coarse | 0.75 | 0.8240 | 131.81 | -0.0920 |
| Medium | 0.34 | 0.8415 | 121.88 | -0.0945 |
| Fine | 0.17 | 0.8436 | 120.11 | -0.0948 |
| Superfine | 0.081 | 0.8433 | 119.54 | -0.0946 |
| Finest | 0.041 | 0.8423 | 119.22 | -0.0944 |

non-uniqueness.

While the occurrence of non-unique solutions is a concern, it is worth mentioning that Jetstream and its 2D predecessor Optima2D [15] have been used to solve many transonic optimization problems in the past, without observing non-uniqueness or the associated convergence difficulties [53, 54, 42, 55, 56, 3]. The phenomenon only seems to arise under very specific flow conditions that produce a sufficiently ill-posed problem. When the flow conditions are adjusted to a Mach number of 0.75 and lift coefficient constraint of 0.6, non-unique solutions are no longer observed during optimization.

To sum up the results for this case, the airfoil with lowest drag is obtained with 16 design variables on each surface. To establish grid convergence for this final geometry, a grid refinement study is performed at the final angle of attack of 2.708°, and the results are presented in Table 3.6. A $C_l$ of 0.8423 and a $C_d$ of 119.22 drag counts are computed on the finest mesh. For comparison, the lowest drag FFD geometry, which is obtained using 11 non-uniformly distributed design variables per side, gives a $C_l$ of 0.8420 and a $C_d$ of 119.38 drag counts on the finest mesh. When control points are clustered towards the leading and trailing edges, the two geometry control methods perform equally well.

## 3.3 Case 3: Twist Optimization of a Rectangular Wing in Inviscid Subsonic Flow

### 3.3.1 Optimization Problem

The optimization problem is the drag minimization of a rectangular wing with zero-thickness trailing edge NACA 0012 sections in inviscid, subsonic flow. The freestream Mach number is 0.5. The design variables are the twist of sections along the span about the trailing edge. Twist is performed by allowing the $z$-coordinates of the B-spline surface or FFD control points to vary under linear constraints, thus linearly shearing the sections. The twist at the root section is allowed to vary, while the angle of attack is fixed. The target lift coefficient is 0.375. The twist distribution should produce a lift distribution close to elliptical and an efficiency factor close to unity. The problem can be summarized as

$$\begin{aligned} &\text{minimize } C_D \\ &\text{w.r.t. } \gamma(y) \\ &\text{subject to } C_L = 0.375 \end{aligned}$$

where $C_D$ and $C_L$ are the drag and lift coefficients, respectively, and $\gamma(y)$ is the twist distribution along the span.

### 3.3.2 Initial Geometry

The initial geometry is a rectangular, planar wing with NACA 0012 sections. The trailing edge is sharp. The semi-span is $3.06c$, with the last 0.06 leading to a pinched tip. Although the tip geometry is not quite consistent with the ADODG case description, which specifies a rounded tip, the main purpose of optimizing the twist distribution is still maintained.

### 3.3.3 Grid

An H-H-topology grid is used for this case. It is a flat-plate grid that is inflated to the NACA 0012 section using the mesh movement algorithm. The optimization level mesh

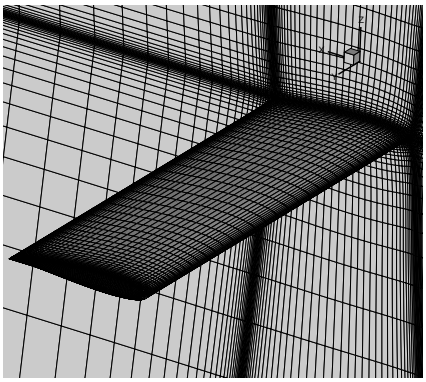

Figure 3.21: Case 3 - Mesh for aerodynamic surface and symmetry plane

Table 3.7: Case 3 - Grid parameters for the rectangular planar wing grid study

| **Grid** | **Nodes** | **Off-wall Spacing (c)** | **Leading-Edge Spacing (c)** | **Trailing-Edge Spacing (c)** |
|---|---|---|---|---|
| Coarse | 1,361,976 | $3\times10^{-3}$ | $3\times10^{-3}$ | $3\times10^{-3}$ |
| Medium | 10,895,808 | $1.5\times10^{-3}$ | $1.5\times10^{-3}$ | $1.5\times10^{-3}$ |
| Fine | 36,773,352 | $1\times10^{-3}$ | $1\times10^{-3}$ | $1\times10^{-3}$ |
| Superfine | 87,166,464 | $7.5\times10^{-4}$ | $7.5\times10^{-4}$ | $7.5\times10^{-4}$ |

on the aerodynamic surface and symmetry plane is displayed in Figure 3.21. To establish grid convergence, the optimization level grid is refined by a factor of 2, 3, and 4 in each direction, giving the grid family with parameters shown in terms of chord units in Table 3.7. The locations of the new nodes added during refinement preserve the hyperbolic nodal distribution.

On the optimization grid, an angle of attack of 4.2040° gives the desired $C_L$ of 0.375 and is used for the grid study. Coefficients of drag and lift, as well as span efficiency factor, are plotted in Figure 3.22 for the different grid levels. The medium and superfine grids, which differ in grid size by a factor of 2 in each direction, give $C_D$ values within 1 drag count of each other. The three finest grid levels appear to be in the asymptotic region, as the behaviour of both functionals is linear with respect to $N^{-2/3}$, where $N$ is the total number of grid nodes, and the spatial discretization is second-order. The span efficiency factor of the initial geometry is very close to unity on the coarse mesh, but the refinement study shows there is in fact room for improvement. The superfine mesh is

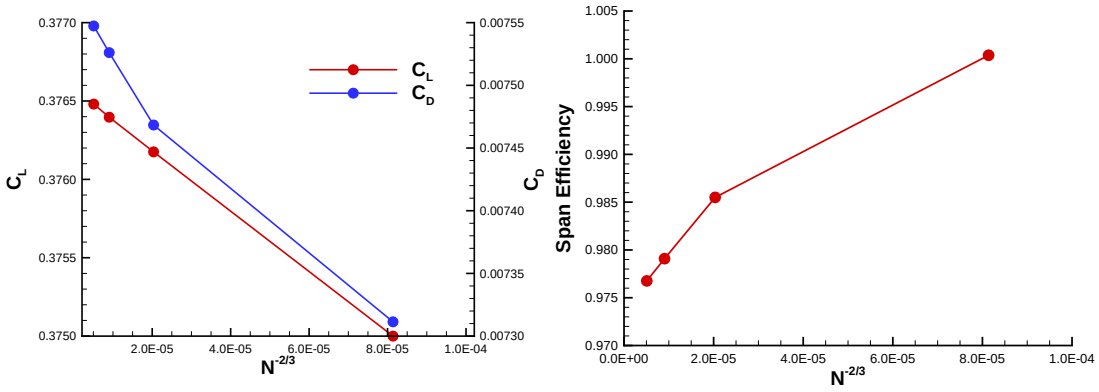


(a) Lift and drag coefficients

(b) Span efficiency

Figure 3.22: Case 3 - Lift coefficient, drag coefficient, and span efficiency factor evaluated on the different grid levels for the initial geometry

chosen for refined analysis of the optimized geometries.

### 3.3.4 Geometry Control Setup

For the B-spline surface optimizations, the twist for the spanwise stations on the tip patches is constrained to be a linear extrapolation of the twist between the two adjacent stations on the inboard patches. This prevents the optimizer from exploiting the surface control point clustering at the tip to create a non-planar feature. This is not necessary for the FFD optimizations since the FFD spanwise stations are sufficiently (uniformly) spaced out along the span. This highlights one of the advantages of FFD's decoupling between the design variables and the surface definition. In some cases, a large number of surface control points may be needed to accurately define a certain geometric feature - in this case, the wing tip cap - but a high degree of geometric flexibility in this region may not be desired. With B-spline surface control, this necessitates additional constraints to be implemented, while with FFD, design variables can be clustered to strategically give fine control only where needed.

For all optimizations, 19 chordwise surface control points per surface are used. For the FFD optimizations, 31 spanwise surface control points are used on the inboard patches. 5 spanwise surface control points are used for the tip patches in all cases to maintain a consistent tip cap geometry. The initial design variables for both 10 design variable cases are displayed in Figure 3.23.

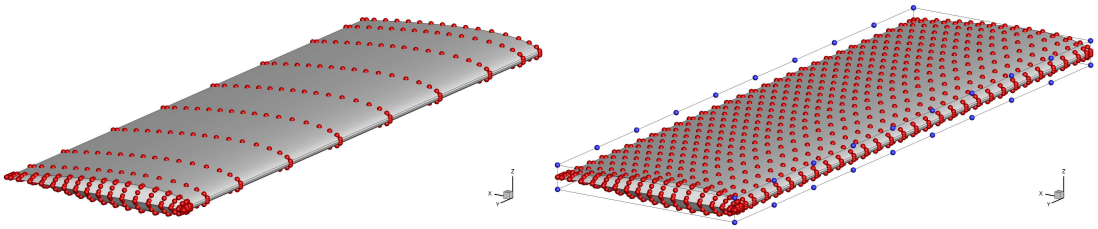

(a) Initial B-spline optimization setup (b) Initial FFD optimization setup

Figure 3.23: Case 3 - Initial 10 twist design variables for B-spline surface (red points) and FFD (blue points) control

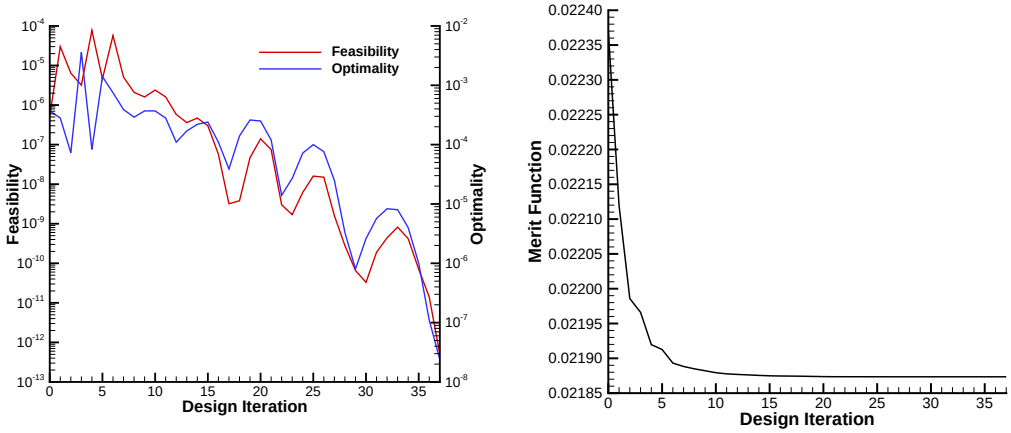


(a) Feasibility and optimality histories (b) Merit function history

Figure 3.24: Case 3 - SNOPT convergence history for the optimization with 10 B-spline surface design variables

### 3.3.5 Optimization Results

The optimizations are conducted on the coarse mesh with different numbers of B-spline surface and FFD design variables. All of the optimizations are successful, reaching feasibility and optimality tolerances of $1\times10^{-6}$ and $1\times10^{-7}$, respectively. For example, the feasibility, optimality, and merit function histories for the optimization with 10 B-spline surface design variables are displayed in Figure 3.24. The final geometries are re-analyzed on the superfine mesh, with the angle of attack adjusted in each case to satisfy the $C_L$ constraint of 0.375. The drag coefficients and span efficiency factors of the initial and optimized geometries are plotted in Figure 3.25. All of the optimized span efficiencies are very close to unity, and the two efficiencies that exceed unity are a reflection of the fact that linear aerodynamic theory does not consider all the effects of the nonlinear Euler equations. For a given number of design variables, the difference in drag between the

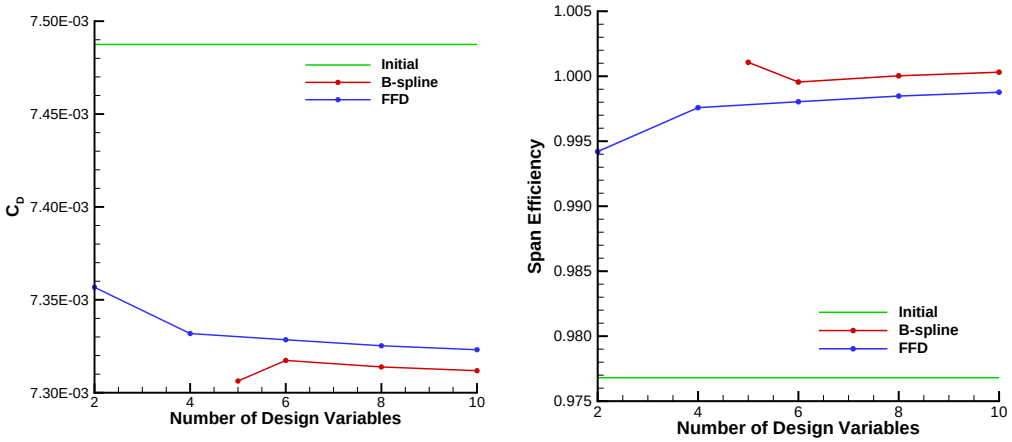


(a) Drag coefficient

(b) Span efficiency

Figure 3.25: Case 3 - Initial and optimized drag coefficient and span efficiency evaluated on the superfine mesh for different numbers of design variables

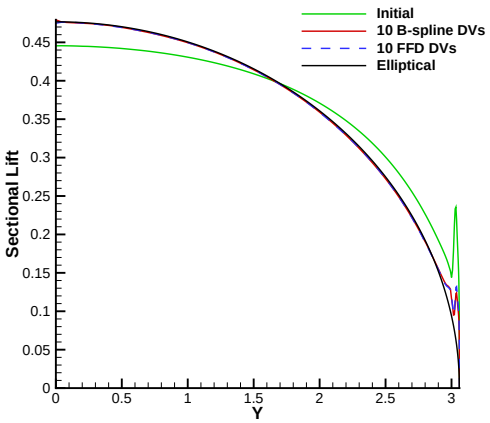


Figure 3.26: Case 3 - Lift distributions from the 10 design variable optimizations, analyzed on the superfine mesh, compared to initial and elliptical distributions

B-spline surface and FFD optimized geometries appears significant, but is actually only about 0.1 counts, as is the deviation of the 5 B-spline design variable data point from the monotonic trend. As expected, the spanwise lift distributions are close to elliptical. For example, the lift distributions obtained with 10 design variables are compared to the initial and elliptical distributions in Figure 3.26. The only noticeable deviation from elliptical occurs at the tip and is attributed to mesh effects at the tip. The distributions from the B-spline surface and FFD optimizations are indistinguishable. The two control methods perform equally well for this case.

## 3.4 Case 4: Twist and Section Optimization of CRM Wing in Turbulent Transonic Flow

### 3.4.1 Optimization Problem

The optimization problem is the drag minimization of the Common Research Model (CRM) wing at a Mach number of 0.85 and a Reynolds number of 5 million, where the reference length is the mean aerodynamic chord (MAC). The lift and pitching-moment coefficients are constrained at $C_L = 0.5$ and $C_M \geq -0.17$, respectively. The moment centre, taken from the wing-body configuration and scaled by the MAC, is taken at (1.2077, 0, 0.007669). Coefficients are calculated using the projected area of 3.407014 squared reference units. The design variables are the $z$-coordinates of the B-spline surface or FFD control points, as well as angle of attack, which is initially set to 2.2 degrees. The trailing-edge surface control points are fixed to permit arbitrary wing twist about the trailing edge, except at the root, where the leading-edge surface control point is fixed. The volume must be greater than or equal to the initial volume of 0.2617 cubed reference units, and the sectional thickness $t$ must remain greater than or equal to 25% of the initial thickness $t_{\text{baseline}}$. The problem can be summarized as follows:

$$\begin{aligned} \text{minimize } & C_D \\ \text{w.r.t. } & z, \alpha \\ \text{subject to } & C_L = 0.500 \\ & C_M \geq -0.17 \\ & V \geq V_{\text{baseline}} \\ & t \geq 0.25 \times t_{\text{baseline}}. \end{aligned}$$

### 3.4.2 Initial Geometry

The initial geometry is the wing of the Common Research Model wing-body configuration from the Fifth Drag Prediction Workshop [57]. The wing has a blunt trailing edge. The wing geometry was obtained by deleting the fuselage, translating the leading-edge root to the origin, and scaling the geometry by the MAC of 275.8 inches [37].

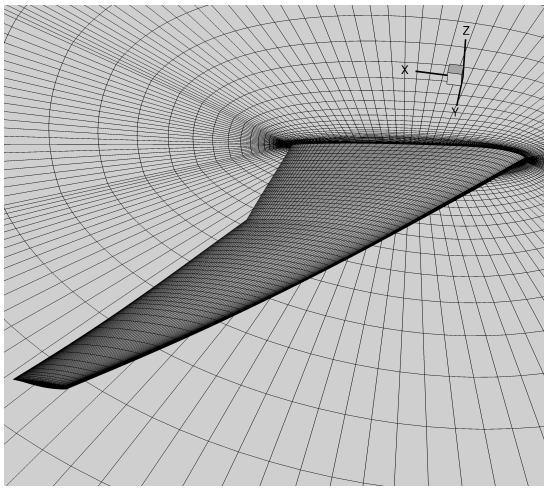


Figure 3.27: Case 4 - Surface and symmetry plane computational mesh for CRM wing geometry

Table 3.8: Case 4 - Grid parameters for CRM wing grid study

| **Grid** | **Nodes** | **Off-wall Spacing (MAC)** | $y^+$ |
|---|---|---|---|
| Coarse | 925,888 | $1.5\times10^{-6}$ | 0.33 |
| Fine | 7,407,104 | $8.1\times10^{-7}$ | 0.17 |
| Superfine | 58,456,064 | $3.9\times10^{-7}$ | 0.081 |

### 3.4.3 Grid

An O-O-topology grid was used for this case. Figure 3.27 shows the coarse grid on the surface and symmetry plane. The coarse grid was refined by factors of 2 and 4 in each direction using parameter refinement to produce fine and superfine grids, and the grid family is described in Table 3.8. The mesh refinement study on the initial geometry, as well as the B-spline surface optimizations and corresponding mesh refinement studies, were conducted by David Koo, another graduate student in the research group. Table 3.9 provides the drag and moment coefficients calculated from the refinement study, with the angle of attack adjusted to give a lift coefficient of 0.5 in each case.

### 3.4.4 Geometry Control Setup

The O-O grid topology gives leading- and trailing-edge patches, which are not compatible with the required top and bottom surface definitions of the region design variable

Table 3.9: Case 4 - Results for CRM wing optimization

| | Optimization Mesh | | Fine Mesh | | Superfine Mesh | |
|---|---|---|---|---|---|---|
| | $C_D$ (counts) | $C_M$ | $C_D$ (counts) | $C_M$ | $C_D$ (counts) | $C_M$ |
| Baseline | 221.6 | -0.174 | 201.5 | -0.175 | 199.1 | -0.175 |
| B-spline surface control | 196.9 | -0.170 | 185.2 | -0.170 | 185.6 | -0.170 |
| FFD control | 199.0 | -0.170 | 186.8 | -0.171 | 185.4 | -0.171 |
| FFD control (medium mesh) | 187.1 | -0.170 | 184.7 | -0.170 | 183.4 | -0.170 |

approach [37], described in Section 2.1.2, for generalizing the treatment of B-spline surface control. As a result, thickness and patch interface continuity constraints must be developed for this specific topology. On the other hand, the FFD formulation does not depend on the topology of the underlying geometry, so no special treatment is needed for the thickness constraints applied to the FFD control points. The thickness constraints are implemented in a more general form that works for arbitrary grid topologies. Nonlinear patch interface continuity constraints are not implemented for FFD since the larger FFD control point spacing relative the surface control point spacing at the interface is expected to give smaller discontinuities.

However, the requirements of fixed trailing-edge and leading-edge root control points are much more easily treated using B-spline surface control. With B-spline surface control, this simply involved giving these control points zero freedom. Since the FFD design variables are the FFD, rather than surface, control points, achieving the same result with FFD is more involved. Due to the volumetric formulation of FFD, to fix the leading-edge root surface control point, a simple constraint only involving the two leading-edge root FFD control points would require that the surface point lie exactly on the leading-edge face of the FFD volume. If instead the surface point lies slightly within the FFD in the chordwise direction, then the embedded point's position becomes affected by the number of FFD control points equal to the order of the volume in that direction. Since the FFD volume is fourth-order in the chordwise direction, the first four top and bottom FFD root control points need to be constrained to fix the embedded point. The same rule applies for embedded points outboard from the root, i.e. to fix the trailing-edge surface

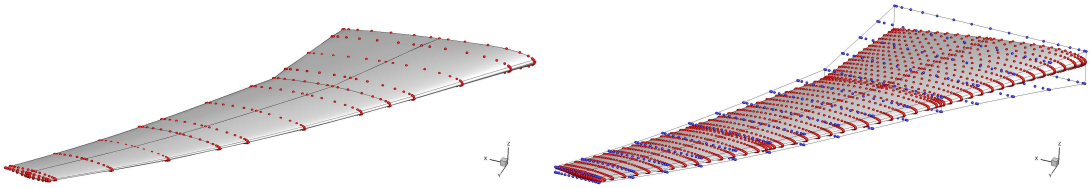

(a) Initial B-spline optimization setup (b) Initial FFD optimization setup

Figure 3.28: Case 4 - Initial design variables for B-spline surface (red points) and FFD (blue points) control

control points. So for the FFD volumes used for this case, which are fourth-, fourth-, and second-order in the chordwise, spanwise, and vertical directions respectively, a general constraint fixing a single embedded point requires constraining $4 \times 4 \times 2 = 32$ FFD control points. The linear equality constraint equation implemented to achieve this comes directly from Equation 2.4, restated here specifically for $z$, the $z$-coordinate of the surface control point of interest, as a function of $B_z$, the $z$-coordinates of the FFD control points:

$$z(\boldsymbol{\xi}) = \sum_{i=0}^{N_i} \sum_{j=0}^{N_j} \sum_{k=0}^{N_k} \mathcal{N}_i^{(p_i)}(\xi) \mathcal{N}_j^{(p_j)}(\eta) \mathcal{N}_k^{(p_k)}(\zeta) B_{z_{i,j,k}}. \tag{3.3}$$

As explained above, the number of non-zero basis function values $\mathcal{N}$ at a given parameter coordinate $\boldsymbol{\xi}$ is determined by the order $p+1$, and this dictates which FFD control points are active in the constraint.

### 3.4.5 Results

For B-spline surface geometry control, the leading-edge patches are parameterized with 5 streamwise by 5 spanwise surface control points, while the rest of the patches are parameterized with 9 streamwise by 5 spanwise points. There are a total of 15 spanwise design sections, and each section is controlled by 35 surface control points. For FFD geometry control, all patches are parameterized with 17 by 17 control points and are embedded inside two FFD volumes joined at the wing crank. The FFD volumes give 15 spanwise design sections, each controlled by 17 chordwise FFD control points on the top and bottom, giving a similar number of design variables to the B-spline surface control setup. The FFD points are clustered towards the leading and trailing edges according to a cosine distribution. The initial design variables for both cases are displayed in Figure 3.28.

Optimizations are conducted using both geometry control methods on the coarse grid. An additional FFD optimization was conducted using the same FFD volume setup but with a medium mesh obtained by refining the coarse mesh by a factor of 1.587 in each direction, giving four times the number of nodes. The results of the optimizations are summarized in Table 3.9, which provides the $C_D$ and $C_M$ computed on the optimization, fine, and superfine mesh levels, with the angle of attack adjusted to give $C_L = 0.5$. On the coarse mesh, B-spline surface control gives lower drag than FFD by about 2 counts. The drag differential essentially disappears, however, when the final geometries are evaluated on the superfine mesh.

The medium mesh FFD optimization gives lower drag than both coarse mesh optimizations by about 2 counts when evaluated on the fine mesh. As expected, there is some advantage to optimizing on a finer mesh, as the optimizer is provided with more accurate flow solutions. This also highlights one of the advantages of FFD. With the current code implementation, increasing the mesh density eventually requires subdividing the blocks to maintain computational efficiency and memory requirements through increased parallelization. Each block is parameterized by fourth-order B-spline volumes, which require a minimum of 5 B-spline control points in each direction. With B-spline surface control, this leads to an increase in the number of design variables. On the other hand, since the FFD volume design variables are decoupled from the geometry surface, the computational mesh density can be increased without modifying the FFD volume and increasing the number of design variables in the process. To achieve the same effect with B-spline surface control requires parallelization at the sub-block level [58] and requires additional code development rather than being an inherent feature of the parameterization.

Upper-surface pressure contours evaluated on the superfine mesh of the initial geometry and those which are optimized on the coarse mesh are displayed in Figure 3.29. On the initial geometry, shocks are visible at the spanwise regions around the crank and near the tip. The shocks are smoothed out by both B-spline surface and FFD optimizations. The FFD and B-spline surface results look largely similar, with the B-spline surface result looking a little smoother in the outboard section. To get a better comparison at precise sections, sectional pressure plots evaluated on the superfine mesh and airfoil sections are plotted in Figure 3.30. The B-spline surface and FFD pressure plots are quite similar, especially for the first five spanwise stations. As previously alluded to, the pressure recovery in the tip region appears somewhat smoother with the B-spline surface result. The regions where there is a shock on the initial geometry are not as smooth on the op-

timized geometry as observed on the coarse mesh, but both control methods give similar features even in these regions. Both control methods have thinned out the sections along most of the wing to reduce wave drag, while thickening the root region significantly due to the thickness constraint. A high degree of sectional control is demonstrated by both parameterizations with the highly cambered leading edges, for example at 26.7% span. Despite the leading-edge root control point being fixed by both cases, the wing from the B-spline surface optimized appears to have higher twist overall, but the final angle of attack is lower.

Figure 3.31 shows the convergence history of SNOPT for the two optimizations on the coarse mesh. The feasibility and optimality tolerances are both set at $1\times10^{-6}$. Optimality is reduced by about two orders of magnitude with respect to its highest value in each case. The differences in initial optimality as well as convergence rate between B-spline surface and FFD control may be due to design variable scaling. Greater reduction in optimality for the B-spline case is possible with further optimization, however the merit function plot shows that most of the drag reduction has already been achieved. The merit function for the FFD optimization is also flattening out, but is not quite as flat. The optimization exited, however, since the optimality tolerance was reached. The FFD optimization was repeated with a lower optimality tolerance, but this affected the convergence path taken by SNOPT and led to poorer convergence and an earlier optimization termination.

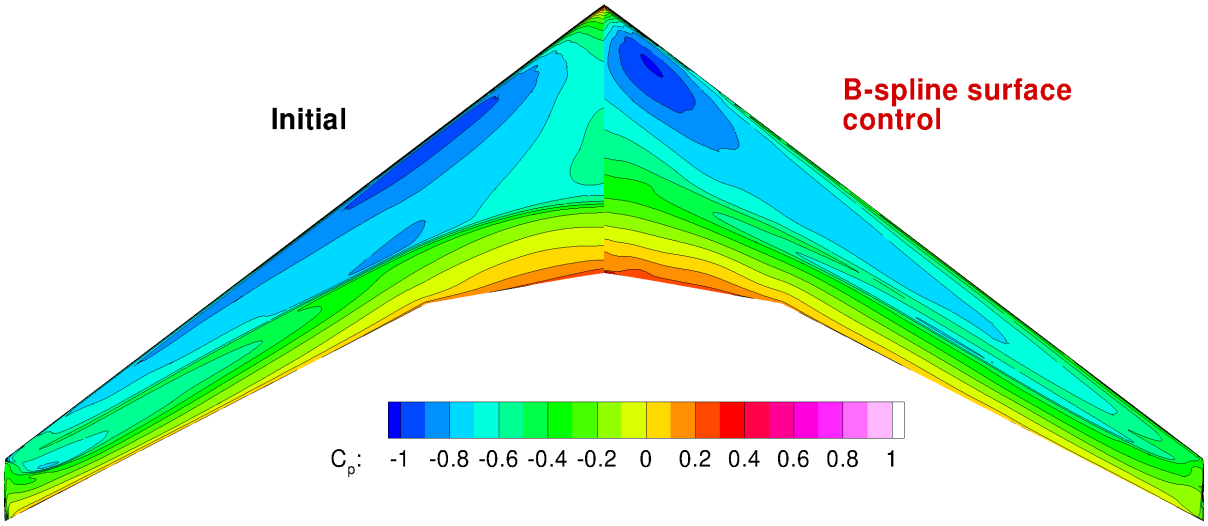


(a) Initial and B-spline control

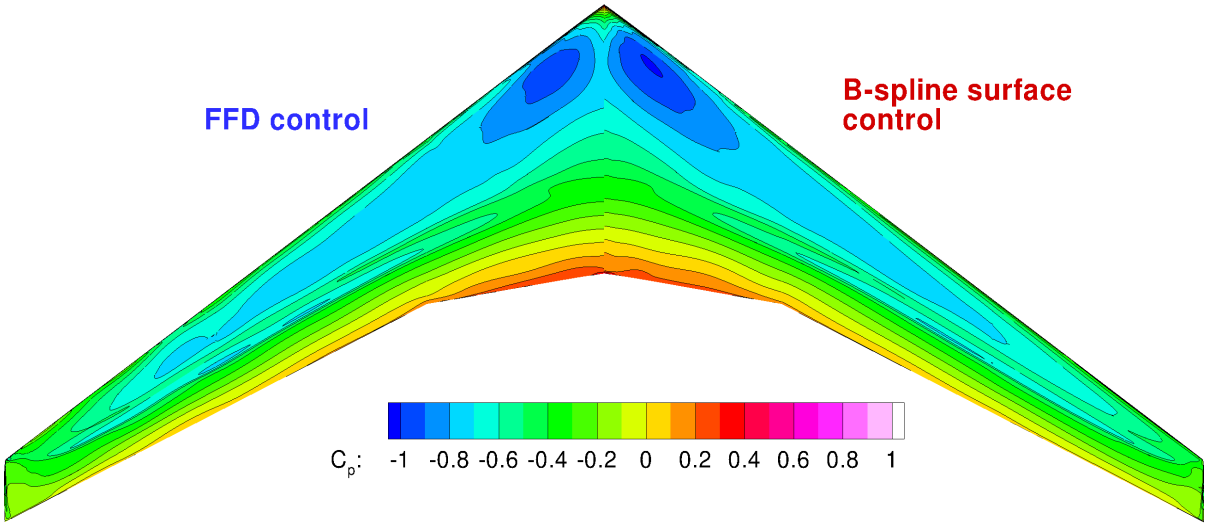


(b) FFD and B-spline control

Figure 3.29: Case 4 - Pressure contours for initial and optimized CRM wing using B-spline surface and FFD control computed on superfine mesh

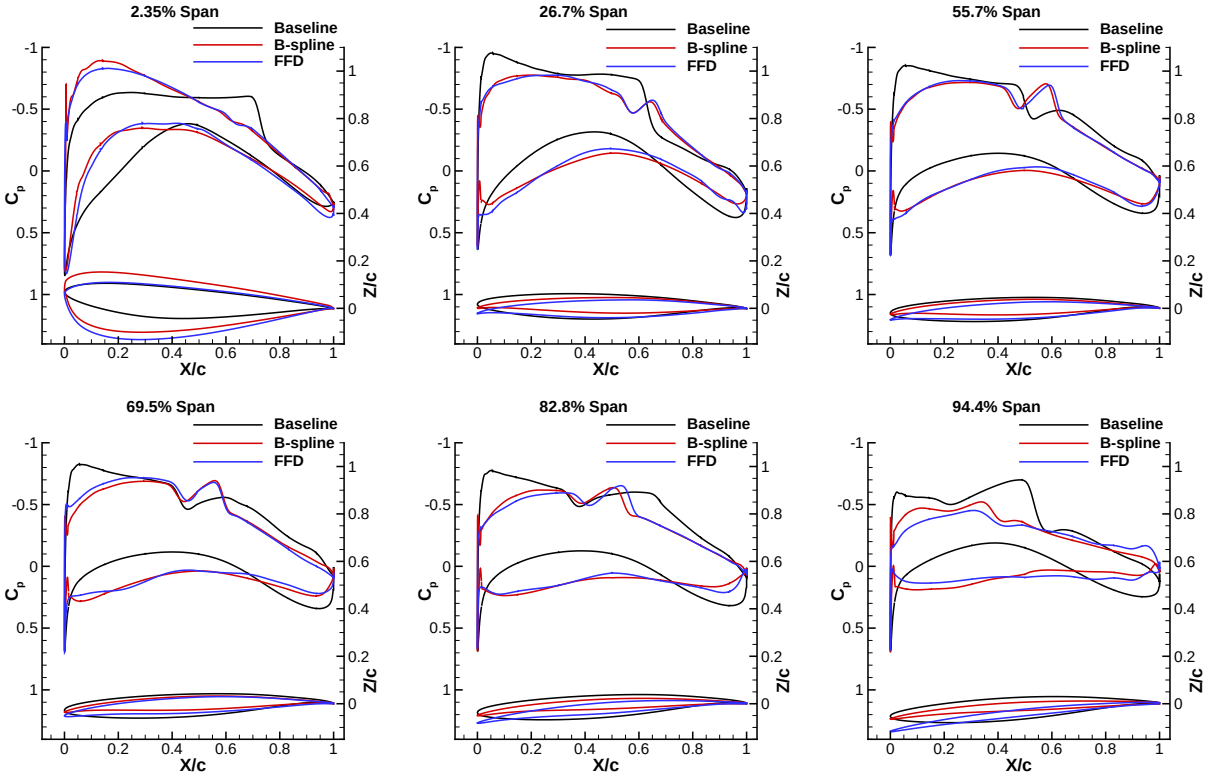


Figure 3.30: Case 4 - Sectional pressure plots and sections for baseline and optimized CRM wings computed on superfine mesh

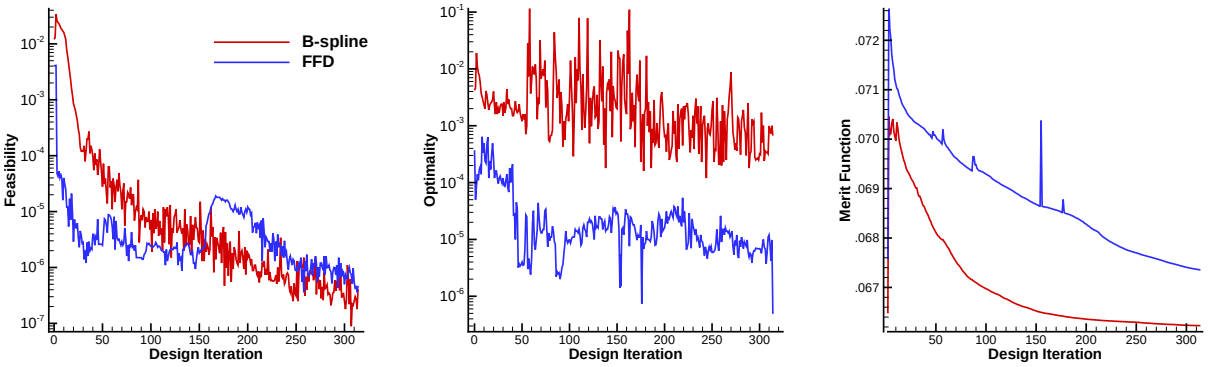


Figure 3.31: Case 4 - SNOPT convergence for coarse mesh optimizations of the CRM wing

## 3.5 Case 5: Exploratory Optimization of a Blended Wing-Body in Turbulent Transonic Flow

### 3.5.1 Optimization Problem

The optimization problem is the maximization of the lift-to-drag ratio of a blended wing-body (BWB) in viscous, transonic flow. The problem is based on the work of Reist and Zingg [59], with the purpose of investigating whether the traditional "home plate" shaped body is still optimal for smaller BWB aircraft. The freestream Mach number is 0.8, and the Reynolds number is 62 million, corresponding to a cruise altitude of 40,000 ft. The design variables include the $z$-coordinates of the B-spline surface or FFD control points, twist about the leading edge, chord, as well as the angle of attack. In addition, the spans of the body and wing can vary, but the total span of 118 ft. and leading-edge sweep are kept constant. To allow this optimization to be exploratory in nature, few constraints are imposed. The body and wing leading edges and wing trailing edges must remain straight. The cabin size requirements are estimated based on the Embraer E190 aircraft. The E190 cabin volume and floor area are estimated to be 5000 ft$^3$ and 770 ft$^2$, respectively. It is assumed that only half of the BWB body can be used for the cabin, and therefore, the body volume and projected area are constrained as $V_{\text{body}} \geq 10,000$ ft$^3$ and $A_{\text{body}} \geq 1540$ ft$^2$, respectively. Due to estimated fuel volume requirements, the wing volume is constrained as $V_{\text{body}} \geq 4500$ gal, where it has been assumed that 80% of the wing volume can be used to store fuel [60]. The design variable and constraint bounds are summarized in Table 3.10. In addition, linear twist on the body and wing is enforced. Linear taper is enforced on the wing, but nonlinear taper is permitted on the body up to deviations of 25% of the current body semi-span.

### 3.5.2 Initial Geometry

The initial geometry, shown in Figure 3.32, is a traditional blended wing-body sized for 100 passengers. The span is limited by ICAO code C gate requirements. The geometry is scaled by the MAC of 40.6 ft.

Table 3.10: Case 5 - Design variable and constraint bounds for BWB optimizations

| **Design Variable** | **Lower Bound** | **Upper Bound** |
|---|---|---|
| Twist | -10° | +10° |
| Chord | -50% | +50% |
| Section | -75% | +100% |
| Body/wing span | -75% | +75% |
| Angle of attack | -3° | +3° |
| **Constraint** | **Lower Bound** | **Upper Bound** |
| Taper ratio | 0.1 | 1.0 |
| Section thickness | -75% | +100% |
| Body projected area | 1540 $ft^2$ | N/A |
| Body volume | 10,000 $ft^3$ | N/A |
| Wing volume | 4500 gal | N/A |

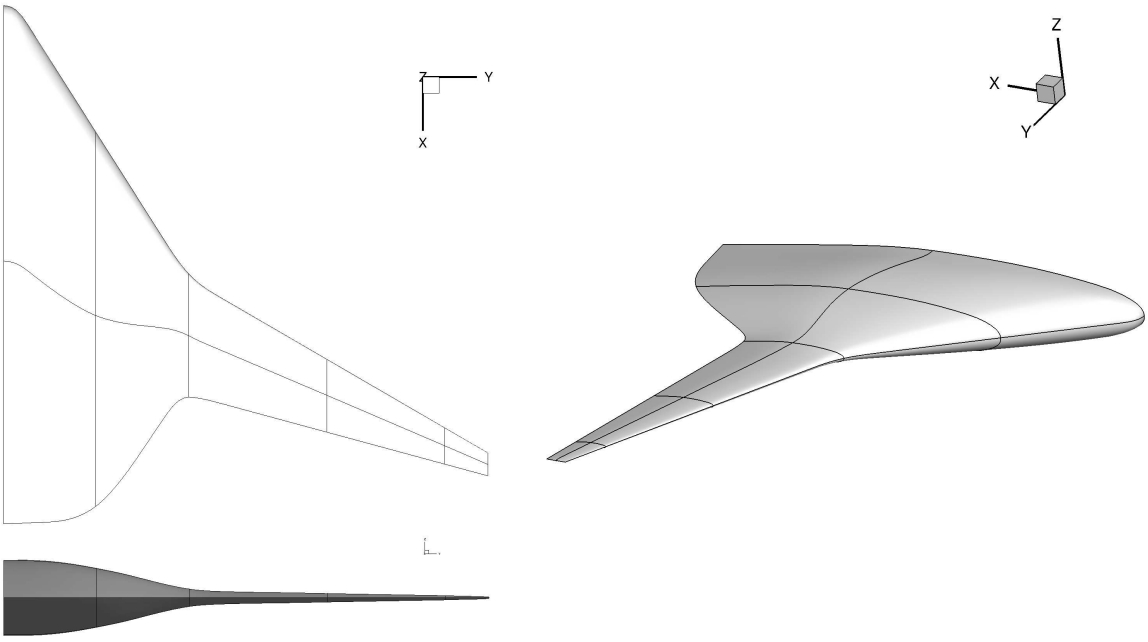


Figure 3.32: Case 5 - Multiple views of initial BWB geometry

### 3.5.3 Grid

An H-O-topology grid is used for this case, and the surface and symmetry plane of the grid used for optimization is displayed in Figure 3.33. The optimization grid is refined

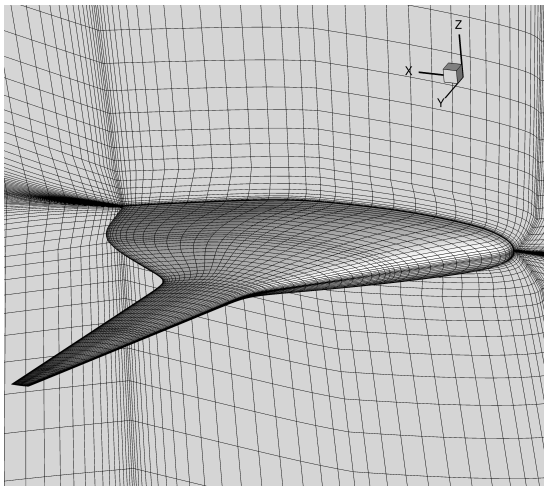


Figure 3.33: Case 5 - Surface and symmetry plane computational mesh for BWB geometry

Table 3.11: Case 5 - Grid parameters for BWB grid study

| **Grid** | **Nodes** | **Off-wall Spacing (MAC)** | $y^+$ |
|---|---|---|---|
| Coarse | 1,225,728 | $1.3\times10^{-6}$ | 2.13 |
| Fine | 9,805,824 | $5.7\times10^{-7}$ | 0.94 |

by a factor of two in each direction, giving the grid parameters shown in Table 3.11. Optimizations are conducted on the coarse grid, and the fine grid is used to analyze the initial and final geometries.

### 3.5.4 Geometry Control Setup

The B-spline surface controlled optimizations are conducted using the region design variable approach [37]; hence no additional setup was required. The body and wing are defined as separate regions. The following constraints had to be added to the FFD code: taper ratio, projected area and volume for the desired regions, fixed sweep for varying region span, and nonlinear taper deviation. All these were implemented in a consistent way to the B-spline surface approach with no additional complexity. The FFD control points are clustered in the chordwise direction according to a cosine distribution. While linear constraints with B-spline surface control are used to ensure the geometry surface intersects the symmetry plane at a perpendicular angle, this is not enforced with FFD.

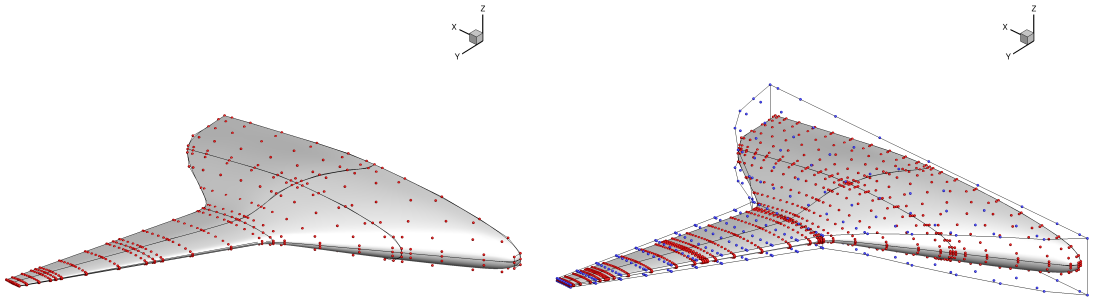

(a) Initial B-spline optimization setup (b) Initial FFD optimization setup

Figure 3.34: Case 5 - Initial design variables for B-spline surface (red points) and FFD (blue points) control

Table 3.12: Case 5 - Results for BWB optimization

| | Coarse Mesh | | | Fine Mesh | | |
|---|---|---|---|---|---|---|
| | $C_L$ | $C_D$ (counts) | $\frac{C_L}{C_D}$ | $C_L$ | $C_D$ (counts) | $\frac{C_L}{C_D}$ |
| Baseline | 0.000 | 96.6 | 0.00 | 0.000 | 84.1 | 0.00 |
| B-spline surface control | 0.298 | 124.2 | 23.96 | 0.306 | 123.9 | 24.67 |
| FFD control | 0.299 | 125.5 | 23.83 | 0.305 | 125.2 | 24.40 |

### 3.5.5 Results

For B-spline surface control, the geometry is controlled using 11 chordwise by 17 spanwise surface control points, while for FFD control, 11 by 17 FFD control points are used. For the FFD optimization, each surface patch is parameterized using 13 chordwise by 9 spanwise control points. The initial design variables for both cases are displayed in Figure 3.34. Optimizations are conducted on the coarse grid, and the functionals for the initial and optimized geometries evaluated on the coarse and fine grids are displayed in Table 3.12. The angle of attack was maintained at the respective design value for the fine mesh analyses: 0.281° for B-spline surface and 2.534° for FFD. Interestingly, while the change in $C_D$ is large, over 12 counts, between the different meshes for the initial geometry, the change is 0.3 counts for the final geometries. This is due to the additional grid resolution necessary to capture the shock on the initial geometry, which is no longer present on the optimized geometries. Hence, the fine-mesh evaluation was deemed sufficiently accurate

for the purposes of the comparison study between the geometry control methods. Recall that the objective function is $\frac{C_L}{C_D}$. The $C_L$, $C_D$, and $\frac{C_L}{C_D}$ ratios are all very comparable between the optimized geometries. The $\frac{C_L}{C_D}$ ratio from B-spline surface control is about 1% higher than that which is achieved using FFD, when analyzed on the fine mesh.

The upper-surface pressure contours, evaluated on the fine mesh, for the initial and optimized geometries are compared in Figure 3.35. The planform of the BWB changes significantly from the traditional "home plate" shape. The root chord increases significantly and a sharper body trailing-edge line is formed. The span of the wing increases, decreasing the span of the body and pushing the wing root more forward. The FFD and B-spline surface optimized geometries are quite similar in planform. The shock that is present on the initial geometry near the wing-body junction is removed in both cases. While the two optimized pressure contours are comparable, the isobars on the B-spline surface controlled geometry are noticeably smoother than on the FFD geometry, which may be indicative of superior sectional control provided by the B-spline surface control.

Sectional pressure distributions, evaluated on the fine mesh, and airfoil sections are displayed at select spanwise stations for the initial and optimized geometries in Figure 3.36. The 2.93% span distributions are quite similar, and the 43.7% span distributions are comparable, but the remaining distributions are quite different. In general, the B-spline surface controlled geometry has smoother pressure distributions.

The SNOPT convergence history is displayed in Figure 3.37. The absence of data at the start of the feasibility plots is due to the feasibility being zero at this stage of the optimizations. The FFD optimality begins and remains lower than that of the B-spline surface optimization, likely due to differences in mathematical definitions of their design variables. Interestingly, the merit functions begin to converge at a near identical rate. Both merit functions level out prior to the onset of mesh movement problems, at which point the optimizations are terminated.

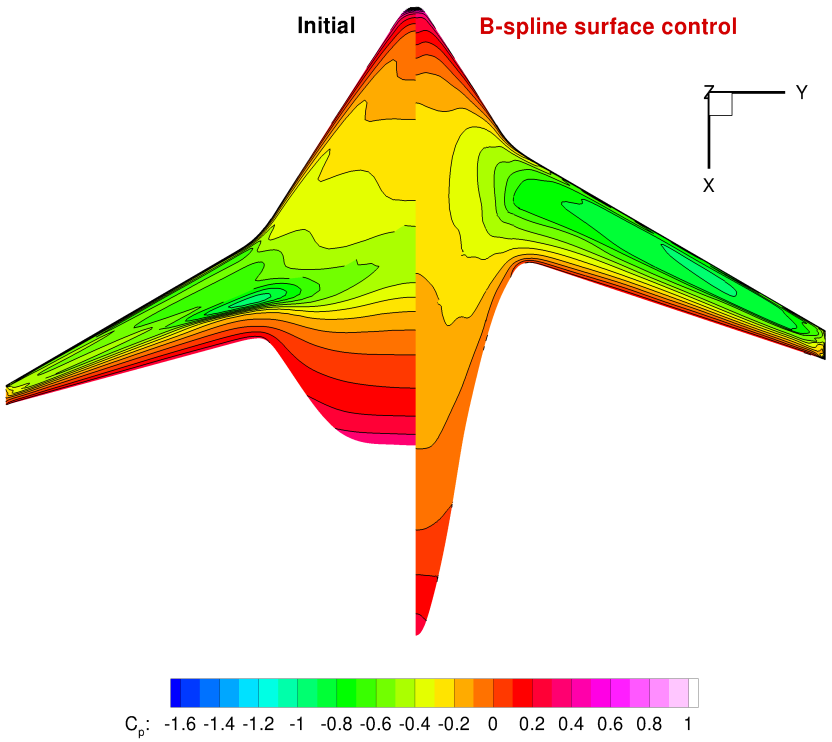


(a) Initial and B-spline control

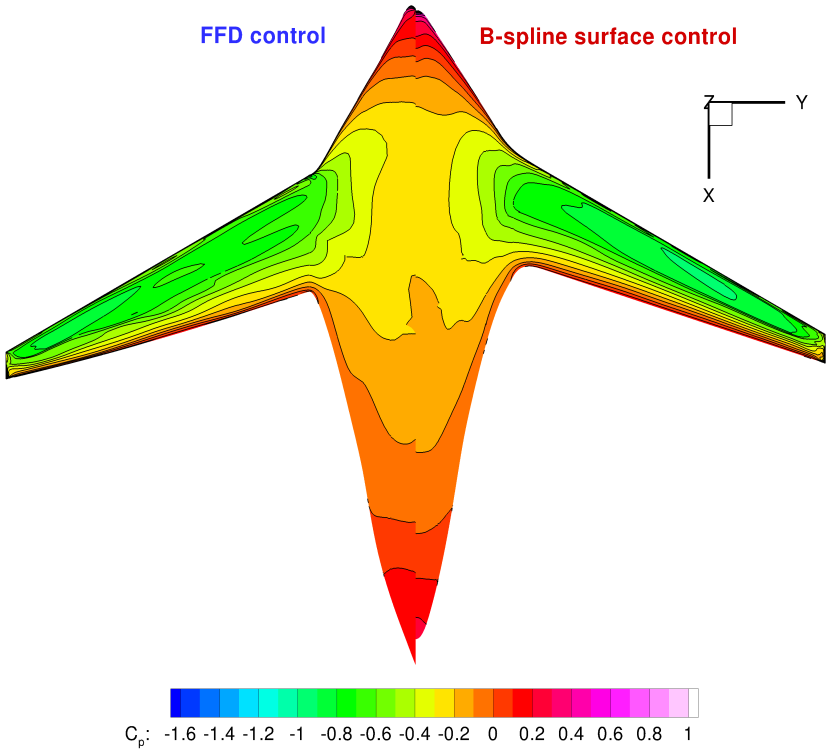


(b) FFD and B-spline control

Figure 3.35: Case 5 - Pressure contours for initial and optimized BWBs using B-spline surface and FFD control computed on fine mesh

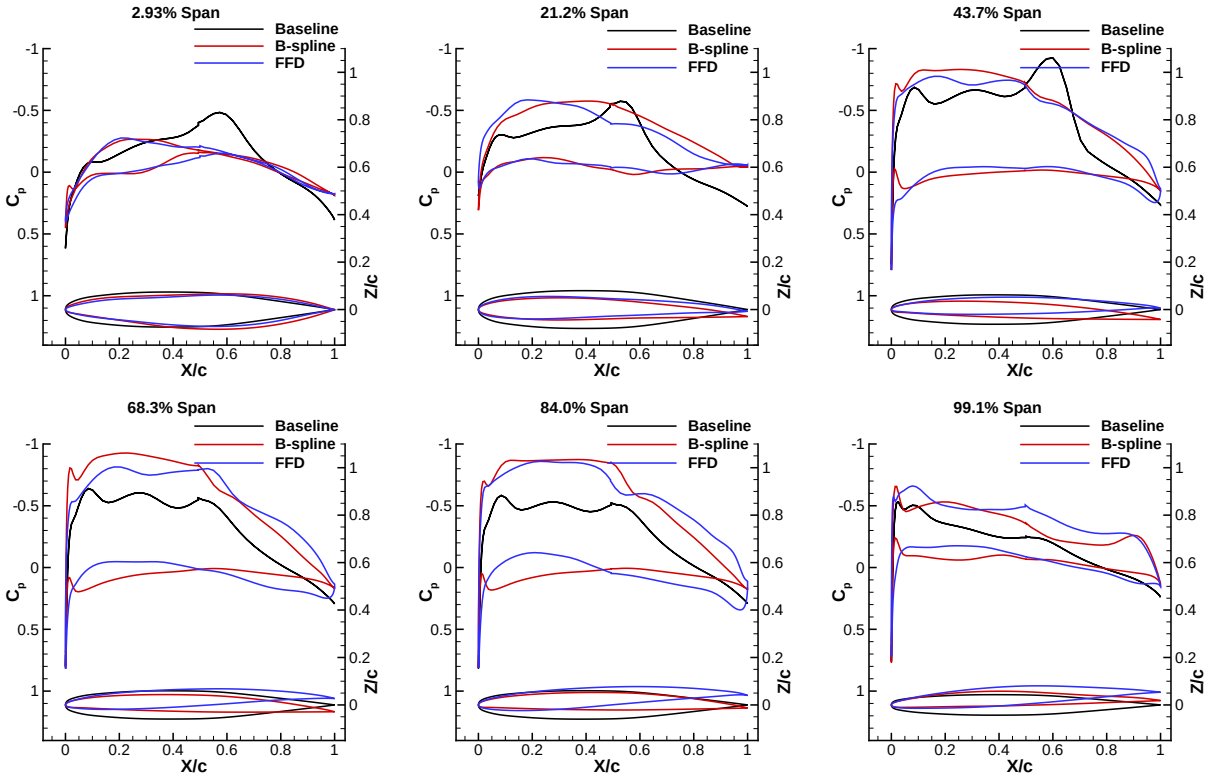


Figure 3.36: Case 5 - Sectional pressure plots and sections for baseline and optimized BWBs computed on fine mesh

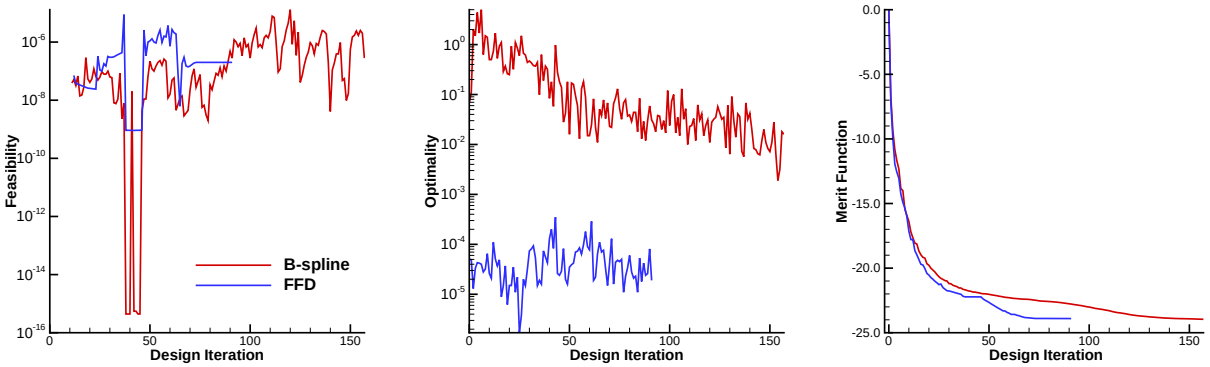


Figure 3.37: Case 5 - SNOPT convergence for BWB optimizations

## 3.6 Case 6: Dihedral Optimization of a Nonplanar Wing in Turbulent Transonic Flow

### 3.6.1 Optimization Problem

The optimization problem is the drag minimization of a nonplanar wing at a Mach number of 0.78 and a Reynolds number of 23.5 million based on the MAC. The lift coefficient is constrained at $C_L = 0.5$. The dihedral, $\Gamma$, is allowed to vary nonlinearly while maintaining constant projected area and span, and is unconstrained. Sectional and angle of attack changes are also permitted. Sectional heights and thickness must remain between 25-400% of their initial values. The volume must be greater than or equal to the initial volume of 0.2275 cubed MAC units. The problem can be summarized as follows:

$$\begin{aligned} \text{minimize } & C_D \\ \text{w.r.t. } & \Gamma, z, \alpha \\ \text{subject to } & C_L = 0.500 \\ & V \geq V_{\text{baseline}} \\ & 0.25 \times t_{\text{baseline}} \leq t \leq 4.00 \times t_{\text{baseline}}. \end{aligned}$$

### 3.6.2 Initial Geometry

The initial geometry is a conventional planar wing with a planform based on the Embraer E190 aircraft. The RAE 2822 airfoil shape is used along the entire wing. The geometry is scaled by the MAC of 13.1 feet. Top and front views of the wing are shown in Figure 3.38.

### 3.6.3 Grid

An H-O-topology grid is used for this case. Figure 3.39 shows the computational grid on the surface and symmetry plane. The grid parameters are shown in Table 3.13. As shall be seen, the conclusions drawn from this case do not necessitate a mesh refinement study.

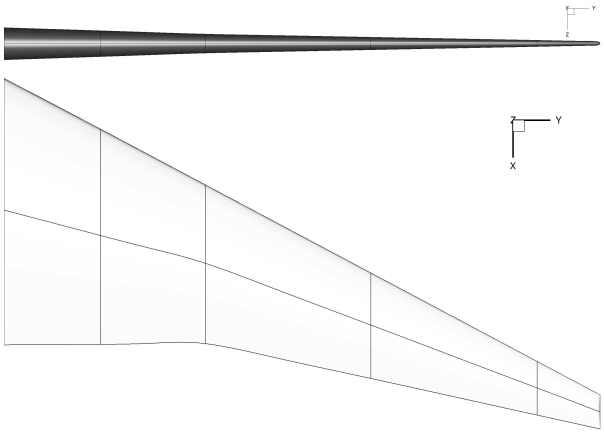

Figure 3.38: Case 6 - Multiple views of initial geometry for nonplanar wing optimization

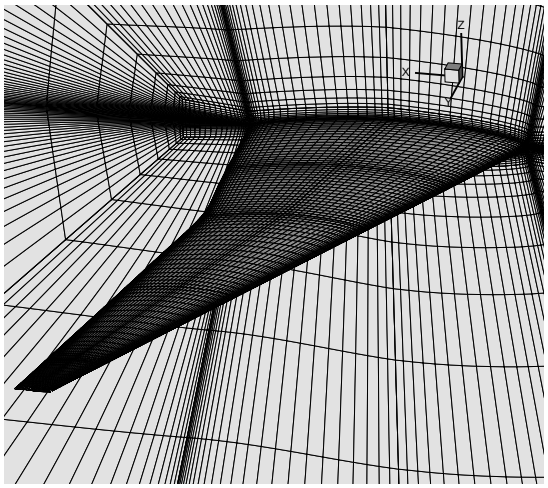

Figure 3.39: Case 6 - Surface and symmetry plane computational mesh for dihedral optimization geometry

Table 3.13: Case 6 - Grid parameters for dihedral optimization grid

| **Nodes** | **Off-wall Spacing (MAC)** | $y^+$ |
|---|---|---|
| 1,452,360 | $1.7\times10^{-6}$ | 1.21 |

### 3.6.4 Geometry Control Setup

The B-spline surface controlled optimization is conducted using the region design variable approach [37] and did not require any additional special setup. A single region is used for the entire wing. A single design variable defines the dihedral as a rotation angle

between the root and tip, and interior sections provide nonlinear dihedral variation. A span design variable is used to maintain constant projected span. The FFD optimization is conducted by allowing the axial curve control points to move vertically and inherently maintains the projected span. The FFD cross-sections are "attached" to the axial curve and rotate to remain perpendicular to the curve.

The minimum possible number of B-spline surface dihedral design variables is inherently tied to the the minimum number of spanwise control point stations required to define the geometry. At least five spanwise stations per block are needed for the cubic B-spline parameterization used. The number of blocks needed is dictated by computational efficiency considerations and memory limitations. Five spanwise blocks, which is typical within the research group for RANS optimizations, gives 21 stations. Since the root is fixed and some of the other stations are constrained to maintain $C^2$ continuity at patch interfaces and $C^1$ continuity at the tip, 11 dihedral design variables remain. Further reduction of the number of design variables requires additional constraints, or a decoupling of the flow analysis and optimization grids [58]. The latter is included in the recommendations for future work in Section 4.2.

On the other hand, the number of axial control points used to control the FFD volume can be chosen independently of the number of surface control point spanwise stations of the underlying geometry. Three FFD volumes enclose the wing: one inboard of the crank, one outboard of the crank, and one at the tip to provide additional clustering of FFD cross-sections where a winglet may form. Each of the FFD volumes is controlled by an axial curve defined by 4 control points. The control points joining the axial curves are constrained to maintain $C^1$ continuity, giving 7 dihedral design variables. In addition, the second last outboard axial control point is free to move outboard up to the span limit of the wing, allowing control over the cant angle of a winglet that may form.

Both B-spline surface and FFD optimizations allow sectional control at 12 spanwise stations, with 11 sectional design variables for the upper and lower surfaces at each section. The FFD control points are clustered towards the leading and trailing edges according to a cosine distribution.

### 3.6.5 Results

Front views of the initial and optimized geometries are shown in Figure 3.40. The FFD optimization produces a winglet-down configuration, while the B-spline optimization pro-

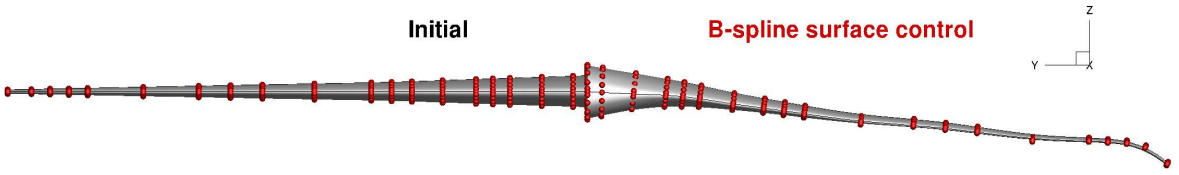


(a) Initial and B-spline optimized geometries

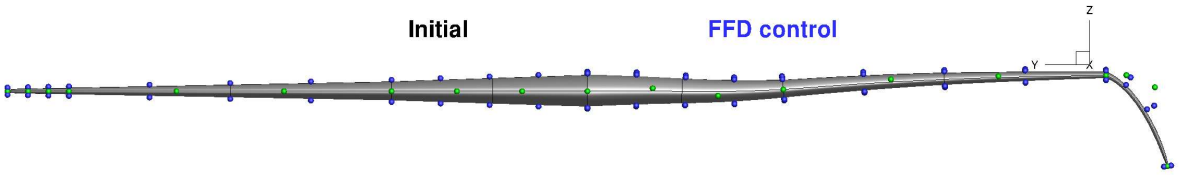


(b) Initial and FFD optimized geometries

Figure 3.40: Case 6 - Front views of initial and optimized geometries. B-spline surface, FFD, and axial control points are shown in red, blue, and green, respectively. Surface control points are omitted in (b) for clarity.

duces more linear anhedral. Interestingly, the tip locations are comparable. The B-spline surface optimization modifies the sections much more than the FFD optimization, thinning the outboard sections and maintaining the wing volume by thickening the inboard sections. This volume redistribution behaviour was also seen during the CRM wing optimizations. In this case, however, the FFD optimization does not redistribute the volume in the same way. The upper-surface pressure contours for the initial and optimized geometries are compared in Figure 3.41. The shock on the initial geometry is removed by both geometry control methods. The pressure contours on the B-spline surface optimized geometry appear somewhat smoother than those on the FFD optimized geometry. The initial and optimized lift and drag coefficients, along with breakdowns into pressure and friction components $C_{D_p}$ and $C_{D_f}$, respectively, are presented in Table 3.14. The optimized $C_L$ values are slightly below 0.500 since projected area $S$ increases marginally due to the rotated tip section extending the projected span by a fraction of the tip thickness, and it is actually $C_L S$ that is constrained based on the initial value of $S$. The FFD optimized geometry has more than 7 counts higher pressure drag than the B-spline surface optimized geometry. The surface area of the FFD optimized wing exceeds that of the B-spline optimized wing by 1.45% and results in higher friction drag. The net result is the B-spline surface optimized geometry giving 8 counts lower drag than the FFD optimized geometry.

The SNOPT convergence history of each case is displayed in Figure 3.42. Both

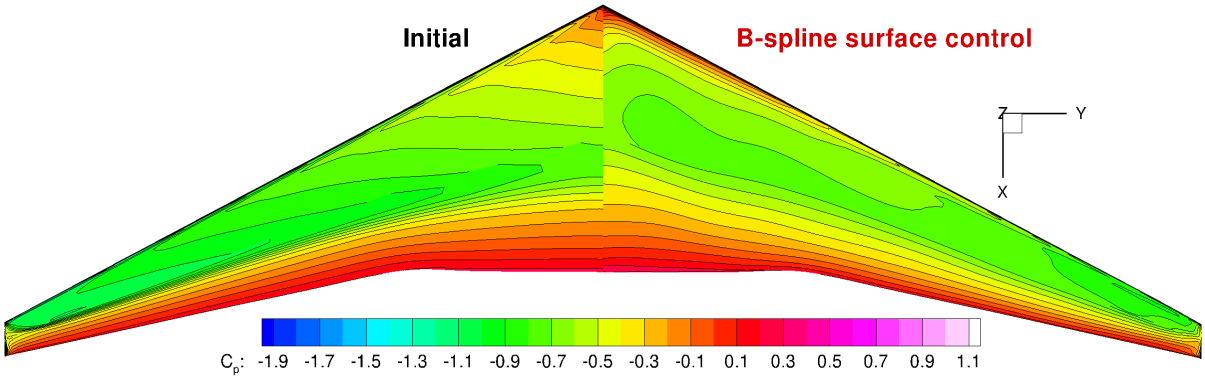


(a) Initial and B-spline control

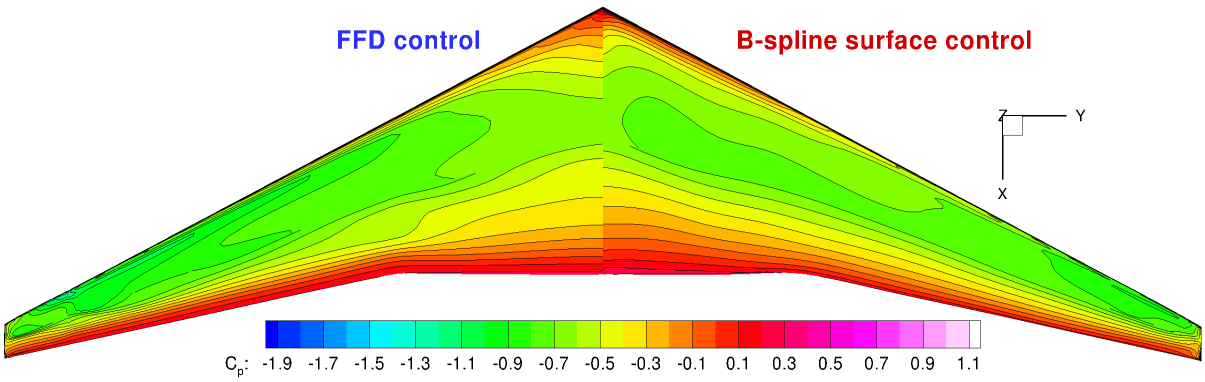


(b) FFD and B-spline control

Figure 3.41: Case 6 - Pressure contours for initial and optimized nonplanar wings using B-spline surface and FFD control

optimizations meet the feasibility tolerance of $10^{-4}$. The B-spline surface optimization reduces optimality by about 1.5 orders of magnitude, and the merit function gets quite flat before mesh movement problems occur. The FFD optimization reduces optimality by 2 orders of magnitude, reaching the tolerance of $10^{-6}$, and SNOPT exits successfully. The merit function does not flatten out before the exit. Reduction of the optimality tolerance in an attempt to allow the optimization to continue further leads to convergence problems due to mesh movement failures. It is interesting that the FFD optimization does not follow the same path as the B-spline optimization even though the FFD volume does have the freedom to make the same changes. The resulting designs may be from two different local minima in the design space. To try to steer the FFD optimization in the same direction, design variable scaling was used to decrease the gradient magnitudes of the dihedral design variables by an order of magnitude. This had the expected effect of

Table 3.14: Case 6 - Results for dihedral optimization

| | $C_L$ | $C_D$ (counts) | $C_{D_p}$ (counts) | $C_{D_f}$ (counts) |
|---|---|---|---|---|
| Baseline | 0.500 | 229.8 | 167.7 | 62.1 |
| B-spline surface control | 0.499 | 189.9 | 124.3 | 65.6 |
| FFD control | 0.499 | 197.9 | 131.6 | 66.3 |

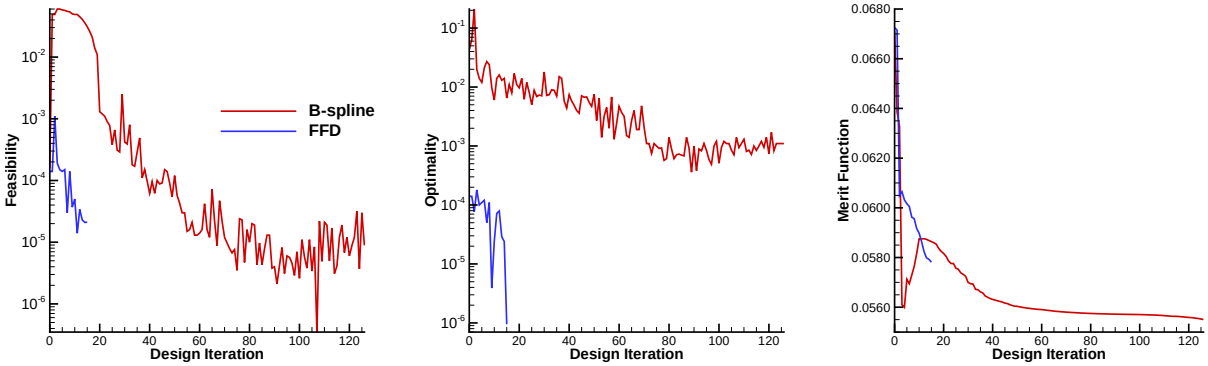


Figure 3.42: Case 6 - SNOPT convergence for dihedral optimizations

producing significantly less dihedral, but the sectional changes were still not comparable to the B-spline optimization and the final drag was higher than when the initial scaling was used.

In summary, the geometries generated by the two geometry control methods are significantly different for this case, and the B-spline optimization gives significantly lower drag. Even when efforts are made to allow the FFD optimization to converge further or to steer the geometry changes in the same direction as the B-spline optimization, the FFD optimization remains outperformed.

# Chapter 4

# Conclusions and Recommendations

## 4.1 Conclusions

B-SPLINE surface control and free-form deformation geometry control methods have been compared in their application to high-fidelity aerodynamic shape optimization. The two geometry control methods have been evaluated by their application to a series of benchmark ASO problems defined by the ADODG, as well as two exploratory optimizations. Similar drag reduction was achieved using both geometry control methods for both the NACA 0012 inviscid, transonic and RAE 2822 viscous, transonic optimizations, when control points were clustered towards the leading and trailing edges. The convergence of these optimizations was impeded by the occurrence of non-unique solutions. The inviscid, subsonic wing twist optimization showed both control methods successfully giving elliptical lift distributions and span efficiency factors very close to unity. The viscous, transonic CRM wing optimization showed B-spline surface control giving 2 counts lower drag on the coarse mesh used for optimization, but this difference disappears when both geometries are analyzed on a finer mesh. The exploratory BWB case showed the B-spline surface control giving a slightly higher lift-to-drag ratio. The nonplanar wing optimization showed the two geometry control methods taking different convergence paths and the B-spline surface optimization more effectively reducing drag. With the exception of this final case, both geometry parameterizations performed equally well, with discrepancies in objective function mitigated through grid refinement. The B-spline surface control gave smoother pressure contours than FFD for the three 3D RANS optimizations. If a single method must be chosen on the basis of aerodynamic performance, B-spline surface control proved to consistently give lower objective function values and smoother pressure

distributions.

With regard to problem setup, each control method has some advantages. As shown with the RAE 2822 case and more clearly with the CRM wing case, fixing specific points on the geometry is more easily achievable with B-spline surface control. B-spline surface design variables can simply be forced to have zero freedom, while the FFD requires the addition of a constraint for each fixed embedded surface point. However, the decoupled definition of an FFD volume from the geometry parameterization allows it to be used more readily with an arbitrary grid topology, as shown with the CRM case. The constraints on the rectangular prismatic FFD volume can more generally be implemented than equivalent constraints for different grid topologies. In addition, an FFD volume can be strategically designed to give fine control only where desired, defining the spacing of the FFD control points independently of the surface control-point clustering that may be needed to capture the geometry accurately. As seen with the twist case, this can avoid the need to implement additional constraints to restrict undesired control. Hence, so long as a constraints involving specific points on the geometry are not a concern, FFD's generality and decoupled nature from the underlying geometry make it a more attractive approach for problem setup.

## 4.2 Recommendations

Based on the current findings, the following are some recommendations for future work:

- **Adaptive FFD control:** FFD's decoupled nature from the underlying geometry lends itself well to adaptivity and progressive refinement. A previous adaptive parameterization approach using B-spline surface control [61] was restricted by the necessity to use knot insertion; i.e. new surface control points had to be placed in specific locations to not change the underlying surface. On the other hand, a new FFD volume can be created with its control points placed completely arbitrarily and therefore more strategically. Of course, the FFD volume itself would have changed, but the underlying geometry can be re-embedded in this new FFD volume without being modified. The adaptivity can be used to progressively add new FFD control points or simply redistribute them.

- **Geometry-fitted FFD volume generation:** The initial rectangular shape of FFD cross-sections, as seen in Figure 3.15(b) for example, results in less sectional

control offered by the leading- and trailing-edge FFD control points than the mid-chord control points. The larger distance between the FFD and surface control points at the leading and trailing edges means that the FFD points must move farther to achieve a certain change in the surface than if this spacing was reduced. An FFD volume whose faces more closely follow the curvature of the surface may offer improved sectional control.

- **Non-unique solutions:** The occurrence of non-unique solutions was detrimental to the optimization convergences of the 2D airfoil cases. No evidence of non-uniqueness was observed for the 3D cases considered, nor for any other cases conducted by the author's research group in the past. However, non-uniqueness has been observed for some 3D wings created from airfoils that exhibited non-uniqueness, depending on the aspect ratio [28]. A better understanding of what conditions yield a non-unique design space would be informative for future wing optimizations.

- **True 2D optimization capability:** If significant work is to continue on 2D airfoil optimizations, it would be worth enabling Jetstream to perform true 2D optimizations, as opposed to using extruded grids, to improve efficiency.

- **Aerostructural optimization:** Since it has been shown that B-spline surface and FFD geometry control methods perform equally well in many aerodynamic optimization cases, a natural progression of this study would be to extend the comparison of these geometry control methods to aerostructural optimization problems, to see if any new advantages or disadvantages appear when structural considerations are included. An aerostructural optimization framework using B-spline surface control is already under development in the author's research group [62], but extending the FFD implementation for aerostructural optimization has yet to be done.

- **Grid decoupling for flow analysis and optimization:** In the current implementation of Jetstream, each block used in the multiblock structured grid is generally assigned to a single processor for flow analysis and gradient evaluation. The minimum number of blocks used is dictated by computational efficiency requirements and memory limitations. For B-spline surface control, this can result in an excessive number of design variables, since each block must be parameterized by a minimum number of control points. To reduce the number of surface design

variables, a grid with fewer blocks can be used for geometry parameterization and mesh movement, and can then be further subdivided to enhance parallelization for flow analysis and gradient evaluation. This was originally proposed by Osusky [58], but the current implementation of this approach is very case specific and therefore requires generalization to arbitrary grid topologies.

# References


[1] Sobieczky, H., "Parametric airfoils and wings," *Notes on Numerical Fluid Mechanics*, Vol. 68, Vieweg, 1998, pp. 71–87.

[2] Sederberg, T. W. and Parry, S. R., "Free-form deformation of solid geometric models," *13th Annual Conference on Computer Graphics and Interactive Techniques*, No. 4, Dallas, Texas, 1986, pp. 151–160.

[3] Gagnon, H. and Zingg, D. W., "High-fidelity aerodynamic shape optimization of unconventional aircraft through axial deformation," *52nd AIAA Aerospace Sciences Meeting*, No. AIAA-2014-0908, National Harbor, Maryland, 2014.

[4] IATA, "IATA annual review 2013," 2013.

[5] IATA, "Fact sheet: Industry statistics," 2012.

[6] IATA, "IATA annual review 2014," 2014.

[7] Samareh, J. A., "Survey of shape parameterization techniques for high-fidelity multidisciplinary shape optimization," *AIAA Journal*, Vol. 39, No. 5, 2001, pp. 877–884.

[8] Mousavi, A., Castonguay, P., and Nadarajah, S., "Survey of shape parameterization techniques and its effect on three-dimensional aerodynamic shape optimization," *18th AIAA Computational Fluid Dynamics Conference*, No. AIAA-2007-3837, Miami, Florida, 2007.

[9] Castonguay, P. and Nadarajah, S., "Effect of shape parameterization on aerodynamic shape optimization," *45th AIAA Aerospace Sciences Meeting and Exhibit*, No. AIAA-2007-59, Reno, Nevada, 2007.

[10] Campbell, R. L., "An approach to constrained aerodynamic design with application to airfoils," *NASA Tech. Report*, 1992.

[11] Braibant, V. and Fleury, C., "Shape optimal design using B-splines," *Computer Methods in Applied Mechanics and Engineering*, Vol. 44, No. 3, 1984, pp. 247–267.

[12] Farin, G. E., *Curves and surfaces for computer-aided geometric design: A practical code*, Academic Press, Inc., 1996.

[13] Samareh, J. A., "Novel multidisciplinary shape parameterization approach," *Journal of Aircraft*, Vol. 38, No. 6, 2001, pp. 1015–1024.

[14] Hicks, R. M. and Henne, P. A., "Wing design by numerical optimization," *Journal of Aircraft*, Vol. 15, No. 7, 1978, pp. 407–412.

[15] Nemec, M. and Zingg, D. W., "Newton-Krylov algorithm for aerodynamic design using the Navier-Stokes equations," *AIAA Journal*, Vol. 40, No. 6, 2002, pp. 1146–1154.

[16] Hicken, J. E. and Zingg, D. W., "Aerodynamic optimization algorithm with integrated geometry parameterization and mesh movement," *AIAA Journal*, Vol. 48, No. 2, 2010, pp. 400–413.

[17] Gagnon, H. and Zingg, D. W., "Two-level free-form and axial deformation for exploratory aerodynamic shape optimization," *AIAA Journal,* Published online, DOI: 10.2514/1.J053575, November 2014.

[18] Lyu, Z., Kenway, G. K. W., and Martins, J. R. R. A., "Aerodynamic Shape Optimization Investigations of the Common Research Model Wing Benchmark," *AIAA Journal*, Vol. 53, No. 4, 2015, pp. 968–985.

[19] Duvigneau, R., "Adaptive parameterization using free-form deformation for aerodynamic shape optimization," Tech. rep., INRIA, France, July 2006.

[20] Anderson, G. R., Aftosmis, M. J., and Nemec, M., "Constraint-based shape parameterization for aerodynamic design," *7th International Conference on Computational Fluid Dynamics*, No. ICCFD7-2001, Big Island, Hawaii, July 2012.

[21] Amoignon, O., Navrátil, J., and Jiří, H., "Study of parameterizations in the project CEDESA," *52nd AIAA Aerospace Sciences Meeting*, No. AIAA-2014-0570, National Harbor, Maryland, January 2014.

[22] Gagnon, H. and Zingg, D. W., "Two-level free-form deformation for high-fidelity aerodynamic shape optimization," *12th AIAA Aviation Technology, Integration, and Operations (ATIO) Conference and 14th AIAA/ISSMO Multidisciplinary Analysis and Optimization Conference*, No. AIAA-2012-5447, Indianapolis, Indiana, September 2012.

[23] Amoiralis, E. I. and Nikolos, I. K., "Freeform deformation versus B-spline representation in inverse airfoil design," *Journal of Computing and Information Science in Engineering*, Vol. 8, No. 2, 2008.

[24] Drela, M., "XFOIL: An analysis and design system for low Reynolds number airfoils," *Low Reynolds number aerodynamics*, Springer, 1989, pp. 1–12.

[25] Vassberg, J. C., Harrison, N. A., and Roman, D. L., "A systematic study on the impact of dimensionality for a two-dimensional aerodynamic optimization model problem," *29th AIAA Applied Aerodynamics Conference*, No. AIAA-2011-3176, Honolulu, Hawaii, 2011.

[26] Jameson, A., Vassberg, J. C., and Ou, K., "Further studies of airfoils supporting non-unique solutions in transonic flow," *AIAA Journal*, Vol. 50, No. 12, 2012, pp. 2865–2881.

[27] Ou, K., Jameson, A., and Vassberg, J. C., "Airfoils supporting non-unique transonic solutions for unsteady viscous flows," *7th AIAA Theoretical Fluid Mechanics Conference*, No. 2014-2927, Atlanta, GA, 2014.

[28] Ou, K., Jameson, A., and Vassberg, J. C., "Studies of wings supporting non-unique solutions in transonic flows," *7th AIAA Theoretical Fluid Mechanics Conference*, No. AIAA-2014-2928, Atlanta, Georgia, June 2014.

[29] Telidetzki, K., Osusky, L., and Zingg, D. W., "Application of Jetstream to a suite of aerodynamic shape optimization problems," *52nd AIAA Aerospace Sciences Meeting*, No. AIAA-2014-0571, National Harbor, Maryland, 2014.

[30] Lee, C., Koo, D., Telidetzki, K., Buckley, H., Gagnon, H., and Zingg, D. W., "Aerodynamic shape optimization of benchmark problems using Jetstream," *53rd AIAA Aerospace Sciences Meeting*, No. AIAA-2015-0262, Kissimmee, Florida, January 2015.

[31] Bisson, F., Nadarajah, S., and Shi-Dong, D., "Adjoint-based aerodynamic optimization of benchmark problems," *52nd AIAA Aerospace Sciences Meeting*, No. AIAA-2014-0412, National Harbor, Maryland, 2014.

[32] Bisson, F. and Nadarajah, S., "Adjoint-based aerodynamic optimization of benchmark problems," *53rd AIAA Aerospace Sciences Meeting*, No. AIAA-2015-1948, Kissimmee, Florida, 2015.

[33] Anderson, G. R., Nemec, M., and Aftomis, M. J., "Aerodynamic shape optimization benchmarks with error control and automatic parameterization," *53rd AIAA Aerospace Sciences Meeting*, No. AIAA-2015-1719, Kissimmee, Florida, January 2015.

[34] LeDoux, S. T., Vassberg, J. C., Young, D. P., Fugal, S., Kamenetskiy, D., Huffman, W. P., Melvin, R. G., and Smith, M. F., "Study based on the AIAA Aerodynamic Design Optimization Discussion Group test cases," *AIAA Journal,* Published online, DOI: 10.2514/1.J053535, 2014.

[35] Méheut, M., Destarac, D., Carrier, G., Anderson, G., Nadarajah, S., Poole, D., Vassberg, J., and Zingg, D. W., "Gradient-based single and multi-point aerodynamic optimizations with the elsA software," *53rd AIAA Aerospace Sciences Meeting*, No. AIAA-2015-0263, Kissimmee, Florida, January 2015.

[36] Hicken, J. E. and Zingg, D. W., "Induced drag minimization of nonplanar geometries based onthe Euler Equations," *AIAA Journal*, Vol. 48, No. 11, 2010, pp. 2564–2575.

[37] Osusky, L., Buckley, H., Reist, T., and Zingg, D. W., "Drag minimization based on the Navier-Stokes equations using a Newton-Krylov approach," *AIAA Journal,* Published online, DOI: 10.2514/1.J053457, March 2015.

[38] Gagnon, H. and Zingg, D. W., "Geometry generation of complex unconventional aircraft with application to high-fidelity aerodynamic shape optimization," *21st AIAA Computational Fluid Dynamics Conference*, No. AIAA-2013-2850, San Diego, California, 2013.

[39] Lazarus, F., Coquillart, S., and Jancène, P., "Axial deformations: an intuitive deformation technique," *Computer-Aided Design*, Vol. 26, No. 8, 1994, pp. 607–613.

[40] Truong, A. H., Oldfield, C. A., and Zingg, D. W., "Mesh movement for a discrete-adjoint Newton-Krylov algorithm for aerodynamic optimization," *AIAA Journal*, Vol. 46, No. 7, 2008, pp. 1695–1704.

[41] Hicken, J. E. and Zingg, D. W., "Parallel Newton-Krylov solver for the Euler equations discretized using simultaneous-approximation terms," *AIAA Journal*, Vol. 46, No. 11, 2008, pp. 2773–2786.

[42] Osusky, M. and Zingg, D. W., "A parallel Newton-Krylov-Schur flow solver for the Navier-Stokes equations discretized using summation-by-parts operators," *AIAA Journal*, Vol. 51, No. 12, 2013, pp. 2833–2851.

[43] Jameson, A., Schmidt, W., and Turkel, E., "Numerical solutions of the Euler equations by finite volume methods using Runge-Kutta time-stepping schemes," *14th Fluid and Plasma Dynamics Conference*, No. AIAA-81-1259, Palo Alto, California, 1981.

[44] Pulliam, T. H. and Zingg, D. W., *Fundamental algorithms in computational fluid dynamics*, Scientific computation, Springer International Publishing, 2014.

[45] Swanson, R. C. and Turkel, E., "On central-difference and upwind schemes," *Journal of Computational Physics*, Vol. 101, No. 2, 1992, pp. 292–306.

[46] Chernukhin, O. and Zingg, D. W., "Multimodality and global optimization in aerodynamic design," *AIAA Journal*, Vol. 51, No. 6, 2013, pp. 1342–1354.

[47] Nocedal, J. and Wright, S., *Numerical optimization*, Springer series in operations research and financial engineering, Springer-Verlag New York, 1999.

[48] De Sturler, E., "Nested Krylov methods based on GCR," *Journal of Computational and Applied Mathematics*, Vol. 67, No. 1, 1996, pp. 15–41.

[49] De Sturler, E., "Truncation strategies for optimal Krylov subspace methods," *SIAM Journal of Numerical Analysis*, Vol. 36, No. 3, 1999, pp. 864–889.

[50] Hicken, J. E. and Zingg, D. W., "A simplified and flexible variant of GCROT for solving nonsymmetric linear systems," *SIAM Journal on Scientific Computing*, Vol. 32, No. 3, 2010, pp. 1672–1694.

[51] Gill, P. E., Murray, W., and Saunders, M. A., "SNOPT: An SQP algorithm for large-scale constrained optimization," *SIAM Review*, Vol. 47, No. 1, 2005, pp. 99–131.

[52] Cook, P. H., McDonald, M. A., and Firmin, M. C. P., "Aerofoil RAE 2822 - Pressure distributions, and boundary Layer and wake measurements," *Experimental Data Base for Computer Program Assessment*, No. 138, AGARD Advisory Report, 1979, pp. A6–1–A6–77.

[53] Buckley, H. P., Zhou, B. Y., and Zingg, D. W., "Airfoil optimization using practical aerodynamic design requirements," *Journal of Aircraft*, Vol. 47, No. 5, 2010, pp. 1707–1719.

[54] Buckley, H. P. and Zingg, D. W., "Approach to aerodynamic design through numerical optimization," *AIAA Journal*, Vol. 51, No. 8, 2013, pp. 1972–1981.

[55] Osusky, L. and Zingg, D. W., "Application of an efficient Newton-Krylov algorithm for aerodynamic shape optimization based on the Reynolds-Averaged Navier-Stokes equations," *21st AIAA Computational Fluid Dynamics Conference*, No. AIAA-2013-2584, San Diego, California, 2013.

[56] Reist, T. A. and Zingg, D. W., "Aerodynamic shape optimization of a blended-wing-body regional transport for a short range mission," *31st AIAA Applied Aerodynamics Conference*, No. AIAA-2013-2414, San Diego, California, 2013.

[57] Levy, D., Laflin, K., Tinoco, E., Vassberg, J., Mani, M., Rider, B., Rumsey, C., Wahls, R., Morrison, J., Brodersen, O., Crippa, S., Mavriplis, D., and Murayama, M., "Summary of data from the Fifth AIAA CFD Drag Prediction Workshop," *51st AIAA Aerospace Sciences Meeting*, Dallas, Texas, January 2013.

[58] Osusky, L. M., *A numerical methodology for aerodynamic shape optimization in turbulent flow enabling large geometric variation*, Ph.D. thesis, University of Toronto, 2013.

[59] Reist, T. A. and Zingg, D. W., "Optimization of the aerodynamic performance of a blended wing-body regional aircraft," Accepted, Dallas, Texas, June 2015.

[60] Raymer, D. P., *Aircraft design: A conceptual approach*, American Institute of Aeronautics and Astronautics, 5th ed., 2012.

[61] Han, X. and Zingg, D. W., "An adaptive geometry parameterization for aerodynamic shape optimization," *Optimization and Engineering*, Vol. 15, No. 1, 2014, pp. 69–91.

[62] Zhang, Z. J., Khosravi, S., and Zingg, D. W., "High-fidelity aerostructural optimization with integrated geometry parameterization and mesh movement," *56th AIAA/ASCE/AHS/ASC Structures, Structural Dynamics, and Materials Conference*, No. AIAA-2015-1132, Kissimmee, Florida, January 2015.